Title

Study of Bubble Dynamics and Mass Transport in Alkaline Water Electrolysis: Insights From Event-Based Imaging

Author

Park, Jooho

Publication Date

2024

UNIVERSITY OF CALIFORNIA,
IRVINE

Study of Bubble Dynamics and Mass Transport in Alkaline Water Electrolysis: Insights From Event-Based Imaging

THESIS

submitted in partial satisfaction of the requirements
for the degree of

MASTER OF SCIENCE

in Mechanical and Aerospace Engineering

by

Jooho Park

Thesis Committee:
Associate Professor Yoonjin Won, Chair
Professor Jack Brouwer
Professor Iryna Zenyuk

2024

DEDICATION

To my wife

Yeonshim Kim

to my parents

Yoobyeong Park and Sunnam Kim

to my country

in recognition of their love and support

TABLE OF CONTENTS

LIST OF FIGURES

LIST OF TABLES

ACKNOWLEDGEMENTS

I would like to express my deepest gratitude to my committee chair, Professor Yoonjin Won, for granting me this invaluable opportunity to study in this research area. Her guidance and support have led me to successfully complete my master's program.

I would also like to thank to my committee members, Dr. Jack Brouwer and Dr. Iryna Zenyuk, who have provided their invaluable time for reviewing my thesis.

I am so grateful for everything I've received at the University of California, Irvine, especially for the wonderful people who I've worked with. I would like to thank all the members in the Won lab, who assisted me in many ways, including Dr. Youngjoon Suh, Sanghyeon Chang, Nicholas Choi, Saba Farahani, Chuanning Zhao, and Dr. Nhi Quach.

ABSTRACT OF THE THESIS

Study of Bubble Dynamics and Mass Transport in Alkaline Water Electrolysis:
Insights From Event-Based Imaging
by
Jooho Park
Master of Science in Mechanical and Aerospace Engineering
University of California, Irvine, 2024
Professor Yoonjin Won, Chair

As green hydrogen becomes increasingly important for advancing carbon neutrality today, the need for improving the efficiency of water electrolysis is emphasized. Water electrolysis technologies include anion exchange membrane, proton exchange membrane, solid oxide, and alkaline electrolyzers. This research focuses on alkaline electrolyzers. Alkaline water electrolysis is the most established technology but still has rooms for improvement. A major bottleneck in alkaline water electrolysis is the formation of gaseous products during the oxygen evolution reaction. The presence of bubbles on electrodes reduces number of active sites, requiring higher overpotential. It has been known that proper management of bubble dynamics plays a crucial role in enhancing electrolysis performance. Therefore, understanding the dynamics of gas generation from electrochemical processes is vital. However, there is still a lack of knowledge regarding bubble dynamics that hampers electrochemical reactions at high current densities. The knowledge gap derives from the complexity of mass transfer phenomena at high current densities and the challenges of examining intense bubble activity at the electrolyte-electrode interface. Investigating bubble evolution within porous media has been particularly challenging due to the limitations of conventional cameras.

However, advancements in image sensor technology open up new possibilities for unveiling the physics behind these limitations. As one example, event-based cameras utilize an advanced imaging technique that mimics the way biological eyes process visual information. Leveraging the capabilities of event-based cameras, this study provides an in-depth analysis of gas bubble generation during electrochemical processes and its impact on performance during alkaline water electrolysis. For this, we have explored two types of electrodes in this study: flat coppers and porous nickel foams. The findings suggest that poor mass transport in porous media may lead to an increase in local current density at electrolyte-electrode interfaces, which can interactively have a great influence on bubble dynamics and transport. Furthermore, distinct aspects of bubble behaviors at different overpotential regions are characterized using quantitative analysis. The observation indicates that a decrease in bubble release rate is closely related to the transition to a mass transport-dominated regime, possibly caused by intense coalescence at high current densities. Overall, the study has great significance that controlling bubble dynamics during the electrolysis process is essential for improving performance by overcoming mass transport limitations.

Chapter 1: Introduction

1.1 Introduction to Water Electrolysis

Global decarbonization today necessitates a stable supply of renewable energy sources, such as wind and solar, to ensure a sustainable future. However, their supply can be easily influenced by variable environmental conditions. Therefore, it is necessary to have efficient energy storage systems to store surplus energy produced during periods of favorable conditions. This stored energy can then be used during times when weather conditions restrict the conversion of energy [1]. Given that hydrogen has the highest gravimetric energy density, approximately 120MJ/kg [2], and is the most abundant element in the universe, it is considered a valuable energy carrier. In other words, hydrogen can store and deliver significant amounts of energy, making it an efficient option for energy storage and transportation. However, pure hydrogen rarely exists in nature. Hence, it needs to be extracted and processed from compounds containing hydrogen. According to the Global Hydrogen Review 2023 published by the International Energy Agency (IEA), global hydrogen production reached approximately 95 million tons in 2022 [3].

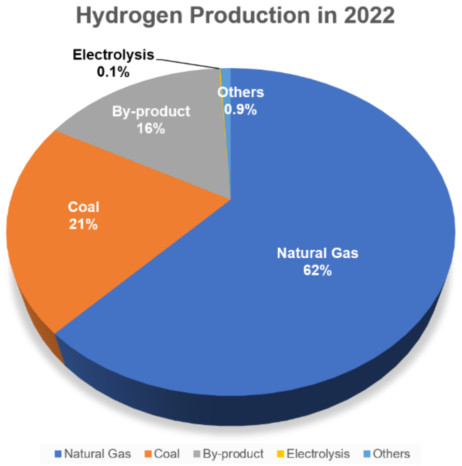

Figure 1. Sources of Global Hydrogen Production in 2022 [3]

The pie chart in Figure 1 reveals that a significant portion of hydrogen production still relies on fossil fuels, accounting for 99%, while only a small fraction around 0.1% comes from water electrolysis. Hydrogen has been used in industries, primarily for ammonia synthesis. As hydrogen applications gain momentum, the demand for hydrogen production is expected to increase by 2% yearly until 2030 [4]. To meet this rising demand, green hydrogen production through water electrolysis needs to expand. Water electrolysis is the process of generating hydrogen and oxygen by splitting water using electric energy. Especially, green hydrogen that can be produced through water electrolysis using renewable energy sources, as shown in Figure 2, is considered as a solution for addressing global decarbonization challenges and meeting future energy needs. This has led to a growing interest in improving the electrolysis performance today.

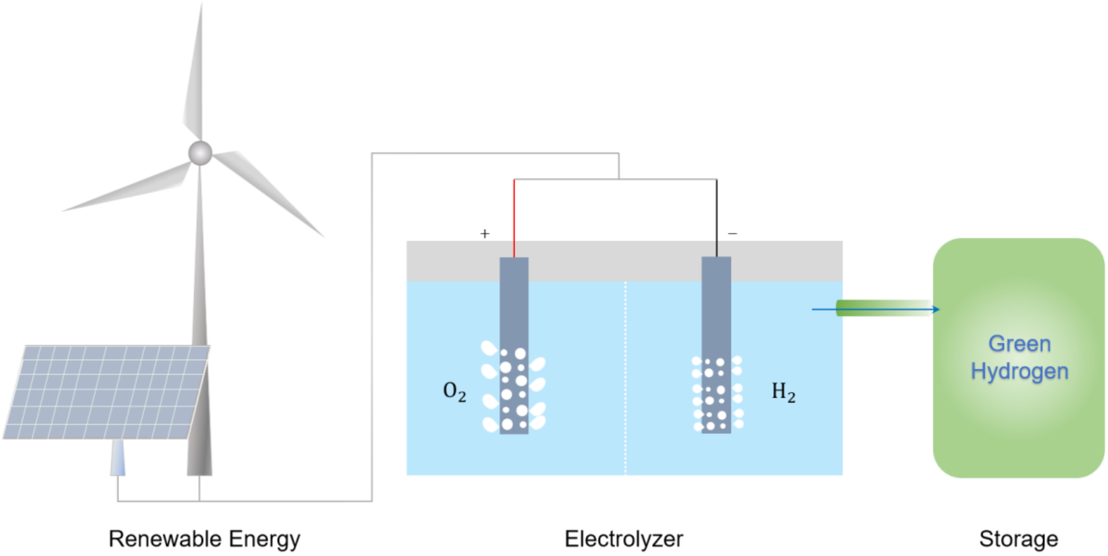

Figure 2. Hydrogen Production via Electrolysis Powered by Renewable Energy

Water Splitting Reaction

The water splitting reaction consists of two half-reactions: a reduction reaction at the cathode (Eq. (1)) and an oxidation reaction at the anode (Eq. (2)). The overall chemical reaction in alkaline water electrolysis is shown in Eq. (3). These reactions generate hydrogen and oxygen gas, respectively.

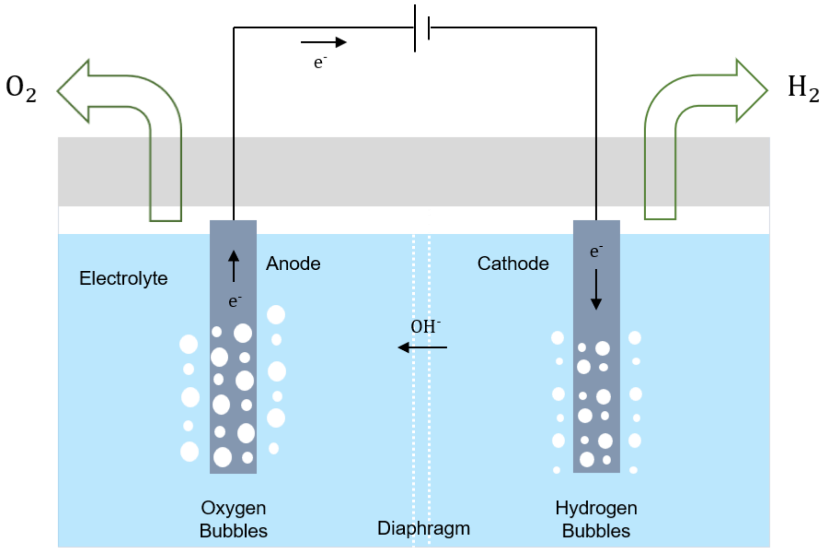

Figure 3. Schematic Diagram of Alkaline Water Electrolysis

- Cathode: $4H_2O + 4e^- \rightarrow 2H_2 + 4OH^-$ Eq. (1)

  Standard state potential: $E^\circ = -0.83\ V\ vs. RHE$

- Anode: $4OH^- \rightarrow 2H_2O + O_2 + 4e^-$ Eq. (2)

  Standard state potential: $E^\circ = +0.40\ V\ vs. RHE$

- Overall reaction: $2H_2O \rightarrow 2H_2 + O_2$ Eq. (3)

  Equilibrium potential: $E^\circ_{cell} = 1.23\ V$

A typical alkaline water electrolysis cell is composed of two electrodes and a diaphragm. The electrochemical cell is placed in a concentrated alkaline solution, such as potassium hydroxide (KOH) or sodium hydroxide (NaOH). A direct current typically flows through the cell, where electrons move from the negative terminal to the cathode. Hydroxide ions undergo oxidation at the anode, releasing electrons and generating oxygen gas [5]. At the cathode, hydrogen gas is produced as water molecules react with electrons.

Overall, the water electrolysis process involves the hydrogen evolution reaction (HER) and the oxygen evolution reaction (OER). The standard potentials in alkaline electrolyzers for both the HER and OER are $-0.83\ V$ and $+0.40\ V$ at 25°C, respectively. The equilibrium potential for the cell is $1.23\ V$. Of the two half-reactions, the OER is known to be the primary obstacle to improving the efficiency of the water splitting process [6-11]. Hence, the study focuses on oxygen gas generation and its impact on electrolysis performance.

Types of Water Electrolyzers

Figure 4 illustrates an overview of four main types of water electrolyzers: (i) alkaline water electrolyzer (AWE), (ii) anion exchange membrane water electrolyzer (AEMWE), (iii) proton exchange membrane water electrolyzer (PEMWE), and (iv) solid oxide electrolyzer cell (SOWE). They are sorted depending on their electrolyte, operating conditions, and their ionic agents [12].

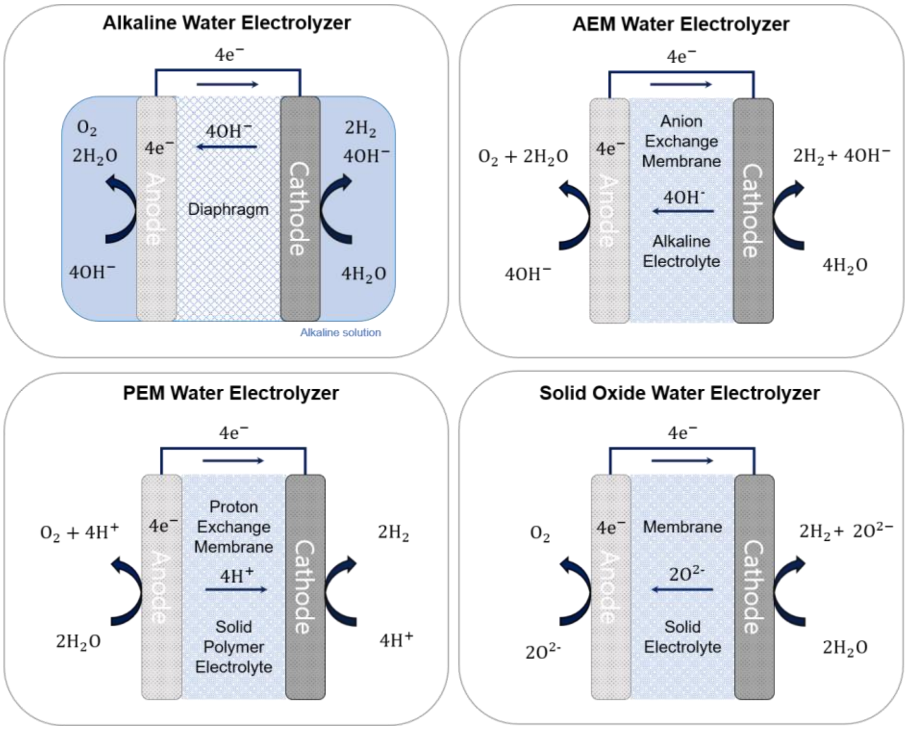

Figure 4. Schematic Diagram of Four Types of Water Electrolyzer [13]

(i) The alkaline water electrolyzer (AWE) is the most well-established and successfully commercialized technology among the four electrolyzers. It is relatively inexpensive and convenient to operate. The electrochemical cell consists of two electrodes separated by a gas-tight diaphragm. The cell is immersed in a highly concentrated alkaline solution (e.g., 5M KOH/NaOH). Hydrogen gas is produced at the cathode as water molecule is hydrolyzed. Hydroxide anion moves through the diaphragm and recombine on the surface of the anode, producing oxygen gas. The AWEs mostly use PGM-free materials. However, they cannot operate under differential pressures and must either be pressurized on both sides or maintain hydrogen at ambient conditions.

(ii) The anion exchange membrane water electrolyzer (AEMWE) is similar to conventional alkaline water electrolyzers in terms of its operating principle in an alkaline solution. However, unlike the conventional AWE, the cathode and anode in an AEMWE are separated by anion exchange membranes instead of diaphragms. In addition, the AEMWE can operate in alkaline solutions with concentrations ranging from 0.1 to 1M. However, the membrane is unstable, and currently, only few electrolyzer suppliers exist for AEM technology.

(iii) The PEMWE operates under acidic conditions. Precious metals, such as platinum or iridium, are commonly employed as electrocatalysts. Water is oxidized at the anode, releasing oxygen, protons, and electrons. The protons move through the membrane to the cathode, where they form hydrogen gas. This technique is commercially available.

(iv) The solid oxide electrolyzer cell (SOEC) typically utilizes ceramic materials, such as yttrium-stabilized zirconia electrolyte (YSZ). The SOEC operates at high temperatures between 700 °C and 850 °C. Under these conditions, water steam is fed to the cathode, where it reacts to form hydrogen gas. The oxide anions generated in the cathode move through the solid electrolyte to the anode. There, they form oxygen gas. The SOEC has advanced to the demonstration level for industrial applications [12].

Table 1: Comparison of Four Types of Water Electrolyzer [12, 14]

	Alkaline	**AEM**	**PEM**	**Solid Oxide**
Electrolyte	KOH/NaOH(5M)	KOH/NaOH(1M)	Solid polymer electrolyte	Yttria stabilized Zirconia (YSZ)
Electrode	Nickel coated stainless steel	Nickel	Iridium oxide, Platinum carbon	Ni/YSZ Perovskites (LSCF,LSM)
Gas diffusion layer	Nickel mesh	Nickel foam Carbon cloth	Titanium mesh Carbon cloth	Nickel mesh/foam
Nominal current density	0.2 - 0.8 A/cm^2	0.2 – 5 A/cm^2	3 – 5 A/cm^2	0.3 – 1 A/cm^2
Voltage range	1.4 – 3 V	1.4 – 2.0 V	1.4 – 2.5 V	1.0 – 1.5 V
Operating temperature	70 - 90 °C	40 - 60 °C	50 - 80 °C	700 - 850 °C
Development status	Mature	Commercialized	Commercialized	R & D

Table 1 compares the four types of water electrolysis technologies. They commonly have considerable rooms for improvement, although many efforts have been made to elevate the energy conversion efficiency. Ideally, if these electrolyzers can operate at higher current densities with less potentials, hydrogen production can increase dramatically. The target current density for alkaline water electrolyzers by 2050 is approximately 4 A/cm^2 [15]. Currently, their operating current densities are below 0.8 A/cm^2. It seems a long way to go, considering the gap between the goal and current conditions. Nevertheless, operating current density has increased over the past few years, due to the findings of efficient electrocatalysts and advancements in electrode surface engineering. To make hydrogen energy more practical and effective, further improvements are necessary. A potential avenue to explore for achieving high current densities is controlling bubble dynamics during the electrolysis process.

1.2 Electrochemical Process Background

1.2.1 Overpotential

The water splitting reaction theoretically requires an equilibrium cell voltage, approximately 1.23V at 25°C, to break water molecules into hydrogen and oxygen. In practice, the required voltage is higher than the theoretical value due to inherent resistances in an electrochemical cell. Additional voltage needed on top of the equilibrium voltage is defined as overpotential. There are three main components that make up the overpotential: activation, ohmic, and mass transport overpotential [10, 16, 17].

$$\eta_{overall} = \eta_{activation} + \eta_{ohmic} + \eta_{mass\ transport} \qquad \text{Eq. (4)}$$

(i) Activation Overpotential

The activation overpotential, also known as the kinetics overpotential, arises from the energy barrier required to overcome prior to electrochemical reaction. It is related to the kinetics of the electron and charge transfer at the electrode surface. The activation overpotential can be represented by the Butler-Volmer equation (Eq. (6)), which is a simplified form of the Current-Overpotential equation (Eq. (5)) [18-21]. The Butler-Volmer equation can be divided into two parts: anodic and cathodic equations (Eq. (7))

$$j = j_0\left(\frac{C_o}{C_o^*}e^{\frac{(1-\alpha)nF\eta}{RT}} - \frac{C_r}{C_r^*}e^{\frac{-\alpha nF\eta}{RT}}\right) \qquad \text{Eq. (5)}$$

$$j = j_0\left(e^{\frac{(1-\alpha)nF\eta}{RT}} - e^{\frac{-\alpha nF\eta}{RT}}\right) \qquad \text{Eq. (6)}$$

$$j_a = j_0 e^{\frac{(1-\alpha)nF\eta}{RT}} \qquad j_c = -j_0 e^{\frac{-\alpha nF\eta}{RT}} \qquad \text{Eq.}(7)$$

where j_a and j_c are anodic and cathodic current density at each electrode; j_0 is the exchange current density; c_o and c_r are the concentration of oxidant and reductant at the electrode surface; c_o^* and c_r^* are the concentration of oxidant and reductant in the bulk; α is the charge transfer coefficient; n is the number of electrons; F is the Faraday's constant; R is the gas constant; T is the temperature.

In the Butler-Volmer equation, it is assumed that the concentration near the electrode surface is equal to the concentration in the bulk, i.e. $\frac{c}{c^*} = 1$. This means that the rate at which mass is transferred is much faster than the rate of the electrochemical reaction. Consequently, the reaction rate is not restricted by the mass transfer [5, 18, 22]. The Butler-Volmer equation can be described to the Tafel equation (Eq. (8)) in cases where the overpotential is large enough, either in cathodic or anodic reactions, to ignore one of the reactions [23].

$$\eta = \frac{RT}{(1-\alpha)nF}\log\frac{j}{j_0}(anodic, when\ \eta \gg 0),\ \eta = \frac{RT}{\alpha nF}\log\frac{j_0}{j}\ (cathodic, when\ \eta \ll 0) \qquad \text{Eq. (8)}$$

In the Tafel equation in Eq. (9), the activation overpotential is a function of current density and the Tafel slope (b) indicates the electrochemical reaction rate. The equation can be estimated by performing Tafel fitting on experimentally measured polarization curves [20, 24].

$$\eta_{act} = a + b\log j \qquad \text{Eq. (9)}$$

(ii) Ohmic Overpotential

The ohmic overpotential is caused by resistances in electrolyte, electrodes, and electric components, including wires and connectors. A significant portion of the resistance is attributed to the presence of ionic transfer resistance within the electrolyte [5, 11, 19, 20]. The ohmic overpotential follows the Ohm's law and increases linearly with current as described in Eq. (10).

$$\eta_{ohmic} = i \cdot R_u \qquad \text{Eq. (10)}$$

R_u represents the uncompensated solution resistance. This ohmic resistance is generally determined by electrochemical impedance spectroscopy (EIS) technique. In practice, the ohmic resistance measured by the EIS technique includes all resistances by the electrode and the electric components, as well as the electrolyte solution [9, 10, 25]. In an electrochemical cell, resistances in the electrode-electrolyte interface can be described by the Randles circuit in Figure 5.

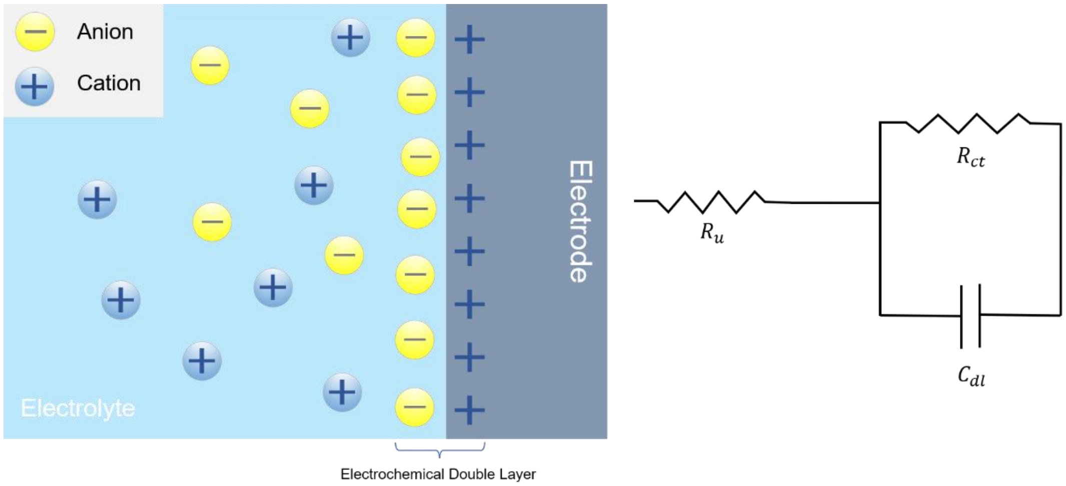

Figure 5. Schematic Diagram of Electrochemical Double Layer [5, 7]

A diagram on the right represents the Randles circuit including an uncompensated solution resistance (R_u), a double-layer capacitance (C_{dl}), and a charge transfer resistance (R_{ct}).

Equation (11) below shows the expression for the impedance in the Randles circuit.

$$Z_{\omega} = R_u + \frac{R_{ct}}{1 + R_{ct}\, C_{dl}(j\omega)} \qquad \text{Eq. (11)}$$

where R_u is the uncompensated resistance; R_{ct} is the charge transfer resistance; C_{dl} is the capacitance of the electrochemical double layer; j and ω represent the imaginary unit and the frequency of applied potential, respectively.

The EIS technique inputs alternating potentials with a set amplitude, scanning from high to low frequencies. When the frequency (ω) is high enough, the denominator in Eq (11) becomes negligible and the solution resistance (R_u) remains. This method is generally used for measuring the solution resistance between the working electrode and the reference electrode.

(iii) Mass Transport Overpotential

As the electrolysis process proceeds to higher current densities, the electrochemical reaction advances to a region where the electrochemical reaction is limited by mass transport. In the region, the rate of electrochemical reactions can diminish by the reduced rate at which reactants move to the electrode surface and gaseous products are removed. This phenomenon causes mass transport overpotential. The mass transport overpotential is significantly affected by the concentration gradient of reactants. The relationship can be expressed by the Nernst equation as shown in Eq. (12) [11, 19, 24].

$$\eta_{mass\ transport} = \frac{RT}{nF} \ln \frac{C_s}{C_{bulk}} \qquad \text{Eq. (12)}$$

where C_s and C_{bulk} are the concentration of reactants on the surface and in the bulk, respectively.

It has been known that mass transport to the electrode is influenced by variations in reactant concentration and micro-convection caused by bubbles [20, 23]. Particularly, previous studies have found that vigorous gas bubble formation has adverse effects on the electrolysis performance. Some studies elucidated how gas bubbles impact the process and explored new approaches to facilitate bubble removal. Iwata et al. (2021) examined the transport overpotential and isolated bubble-induced overpotentials using bubble layer thickness and bubble coverage on the electrode surface [16]. In many studies, the mass transport overpotential is determined by subtracting the activation overpotential and the ohmic overpotential from the total overpotential [10, 16].

Figure 6 presents a typical polarization curve for alkaline water electrolysis, which exhibits three distinct regions: activation overpotential region at lower current density; ohmic overpotential region at moderate current density; mass transport overpotential region at higher current density. The initial increase in potential results from ion-electron transfer kinetics. In the moderate current density region, ohmic overpotential becomes dominant, which linearly increases with current according to the Ohm's law. Finally, when the current density reaches a certain point, there is a steep increase in potential due to mass transport limitations [20].

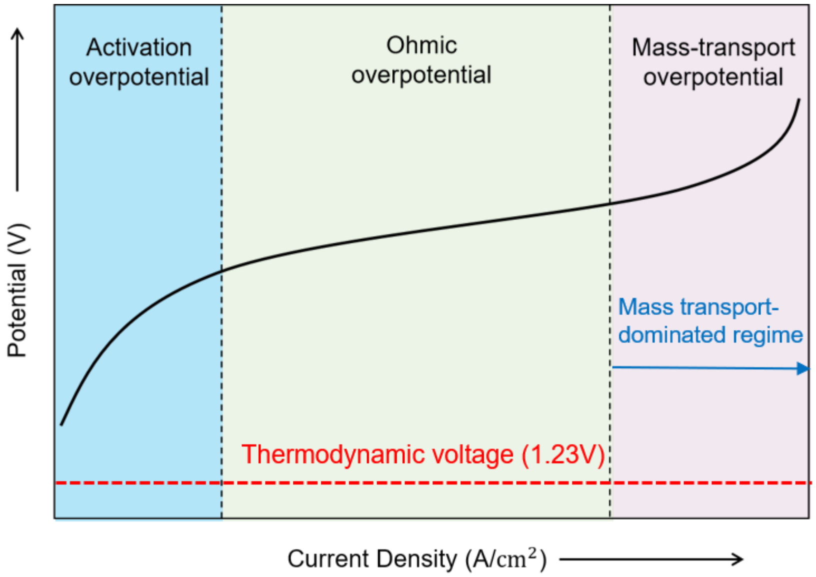

Figure 6. Typical Polarization Curve for Water Electrolysis [20]
The curve is divided into three regions by dominant factors in overpotential. Understanding each contribution to the overall overpotential is crucial for improving electrolysis efficiency.

As mass transport dominates the electrochemical reaction at high current densities, electrolysis performance drastically drops. This regime is called the mass transport-dominated regime and is seen as a main barrier to achieving high efficiency. A key factor to consider in terms of electrolysis efficiency is the voltage efficiency, defined as the ratio of the thermodynamic voltage (V_{th}) to the actual cell voltage (V_{cell}) [21]. In the mass transport-dominated regime, increased overpotentials reduce voltage efficiency. Hence, it is crucial to comprehend the physics behind the transition to the mass transport-dominated regime. However, the exact mechanisms governing this phenomenon remain uncovered [26].

Other factors influencing electrolysis process includes electrolyte concentration, temperature, pressure, electrode's material, spacing between electrodes, electrical material and others [27]. Previous studies have shown that higher cell temperatures improve ionic conductivity and reaction kinetics, resulting in lower overpotential. Furthermore, higher pressure of electrolyte can lead to more efficient electrolysis. Closer distances between electrodes reduce ionic resistance. In addition, promoting bubble release can lower overpotential. Numerous methods have been explored to facilitate the elimination of bubbles, such as the utilization of surfactants, superaerophobic surfaces, flow fields, magnetic fields, and other techniques [28].

1.2.2 Critical Current Density

The critical current density is defined as a turning point on a polarization curve where mass transport overpotential abruptly becomes significant due to poor reactant transport and a sluggish bubble evolution rate. In other words, when current density exceeds the critical point in an electrolytic cell, the efficiency of the cell significantly deteriorates because vigorous bubble generation acts as an insulating layer over the electrode surface, hindering the electrochemical reaction [29]. Thus, the critical current density is considered as the upper limit of operation and a key factor in designing electrochemical systems [30, 31]. Lee et al. (2020) first proposed the concept of critical current density as a performance indicator for gas-evolving electrochemical cell, and they experimentally observed the presence of a critical current density in porous transport layers [26]. As shown in Figure 7, a critical current density is observed prior to reaching a limiting current density. At a certain point during the reaction, bubbles begin to get trapped in the porous transport layer, and the bubbles does not sufficiently release. Consequently, as the bubbles cover the electrode surface, it becomes difficult for reactants to reach the active surface area for the reaction.

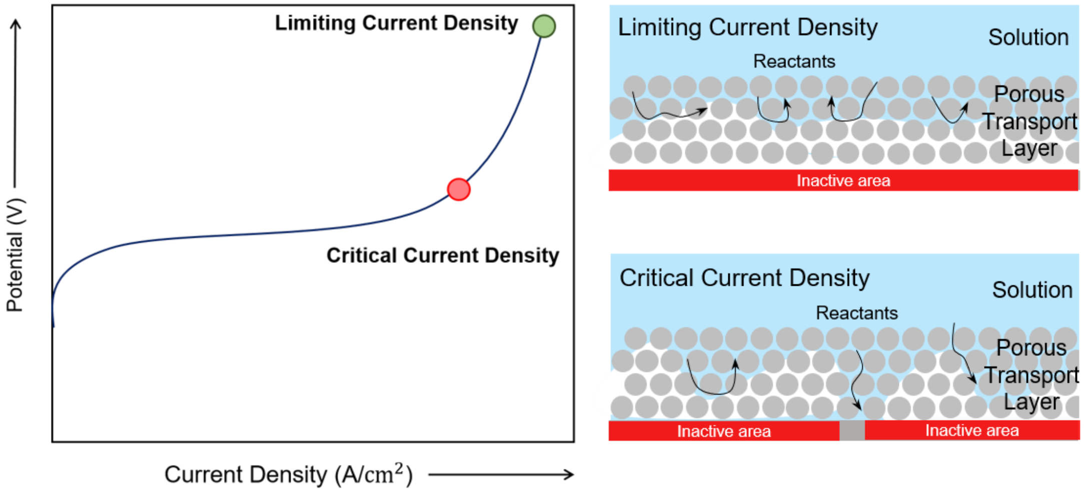

Figure 7. Comparison of Limiting and Critical Current Density [26]
The left side of the figure display a polarization curve, highlighting critical current density (red) and limiting current density (green). As shown in the right diagram, limiting current density is caused by accumulated bubbles within a porous transport layer, hindering the accessibility of reactants to the electrode surface. Critical current density arises prior to limiting current density, featuring a significant increase in potential.

1.2.3 Limiting Current Density

While Lee et al. define the limiting current density as the point where reactions completely stop due to electrode passivation by accumulated bubbles, the more general term refers to the maximum rate of the electrochemical reaction, which is limited by the rate of mass transport of reactants to the electrode surface [23, 26]. The rate of the electrochemical reaction is affected by the concentration gradient of reactants between the bulk solution and the electrode surface. This relationship is described by Equation (13).

$$j = \mathrm{n}Fk(C^* - C) \qquad \text{Eq. (13)}$$

where j is the current density; n is the number of electrons; k is the mass transfer coefficient; F is the Faraday's constant; C^* is the concentration of reactants in the bulk; C is the concentration of reactants at the electrode surface.

The maximum rate of electrochemical reactions occurs when the C approaches zero. At this point, the rate at which the reactants are consumed is much faster than the rate at which they are replenished at the surface. Thus, the limiting current density (j_l) can be expressed using Equation (14). Combining the Equation (13) and (14), overall relationship can be represented by Equation (15) [23].

$$j_l = \mathrm{n}FkC^* \qquad \text{Eq. (14)}$$

$$\frac{C}{C^*} = 1 - \frac{j}{j_l} \qquad \text{Eq. (15)}$$

1.3 Influence of Bubbles on Water Electrolysis Performance

In alkaline water electrolysis, oxygen is evolved at the anode. During the process, gas bubbles are inevitable products of the reaction. Bubble formation is known to influence the electrochemical reaction by covering the effective surface areas, limiting mass transport, and increasing resistances. There have been a number of studies investigating the bubble impacts and addressing their adverse effects [32]. This section presents widely accepted knowledge regarding the influence of bubble generation on electrochemical reactions.

Gas Bubble Evolution

The evolution of gas bubble follows three steps as illustrated in Figure 8: nucleation, growth, and detachment. Fundamentally, a bubble nucleates when a solution near the electrode surface becomes supersaturated with dissolved gas. The supersaturation level is subject to a variety of factors, such as electrode's geometry and wettability, current density, electrolyte, bubble formation, flow field, and others [19, 32]. While bubbles typically nucleate at heterogeneous surfaces, crevices or cavities on the surface tend to make the bubble nucleation easier. After nucleation, the bubble grows by absorbing more dissolved gas molecules nearby. As the bubble grows, the buoyant force on the bubble increases. When the buoyant force overcomes the adhesion force, the bubble detaches from the electrode. Furthermore, several studies have found that the electrostatic force between the charged bubble and the electrode can also influence the bubble diameter at detachment, forcing the bubble to overcome in addition to the buoyant and adhesion forces [24, 33]. Immediately after detachment, the masked surface areas by bubbles are replenished with the solution and reactants, along with micro-convection [34, 35].

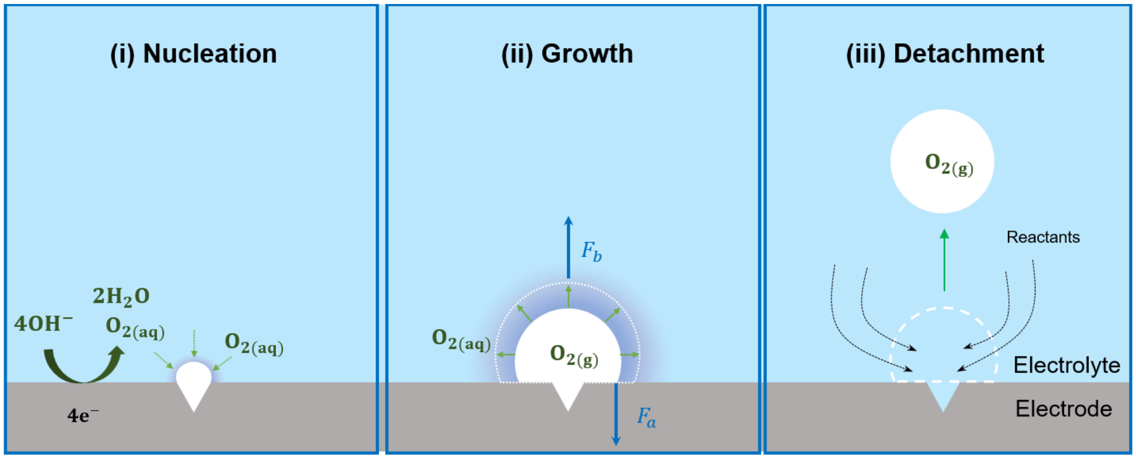

Figure 8. Three Stages of Gas Bubble Evolution. This diagram depicts bubble evolution process during oxygen evolution reaction: (i) Nucleation, (ii) Growth, (iii) Detachment

Bubble Impact on Overpotential

The impact of gas bubbles during water electrolysis is significant for energy efficiency. Much of research has explored the impact of bubbles on overpotential and isolated corresponding individual overpotentials, including activation, ohmic, and mass transport overpotentials. For example, Iwata et al. (2021) measured the thickness of bubble layers on the electrode and the bubble coverage to estimate bubble-induced overpotentials [16]. Dastafkan et al. (2023) demonstrated that a higher surface coverage by bubbles causes an increase in ohmic overpotential [36]. Although there are still ongoing studies to comprehend the exact mechanisms, the commonly accepted knowledge behind this phenomenon is presented here. First, bubbles attached to the electrode surface reduce the active surface area for reactions. Additionally, the attached bubbles cause a localized current density distribution [37]. Second, departing bubbles interrupt the delivery of hydroxide ions from the cathode to the anode, and creates voids within the solution. As a result, departing bubbles worsen the electrolyte's conductivity and increase the ohmic overpotential, particularly in systems using a porous mesh as catalyst layer. Finally, it is known that the bubble emergence reduces the gas supersaturation level near the electrode surface, promoting mass transport. In addition, departing bubbles induce convection and turbulence, enhancing mass transport [24]. Numerous studies have sought to manage these bubble behaviors in favorable ways for electrolysis, such as increasing the number of nucleation sites, reducing the bubble departure size, and accelerating the bubble release rate [11]. However, further investigation is needed to optimize the bubble dynamics during water electrolysis.

Chapter 2: Methodology

2.1 Experimental Setup and Procedures

Figure 9 shows a picture of the complete experimental configuration for a membrane-less electrochemical cell, designed for studying gas-evolving reactions in alkaline water electrolysis. This setup was used for all electrochemical measurements and bubble dynamics studies. The oxygen evolution reaction was investigated using a potentiostat (SP-300, BioLogic). The electrochemical reaction rig comprised a three-electrode cell, which included an acrylic chamber with a lid and a Teflon base. The working electrodes (WE) were positioned in the middle of the cell and connected to a wire that passed through a hole at the bottom of the Teflon base. They were placed approximately 3 cm away from both the reference electrode (RE) and the counter electrode (CE).

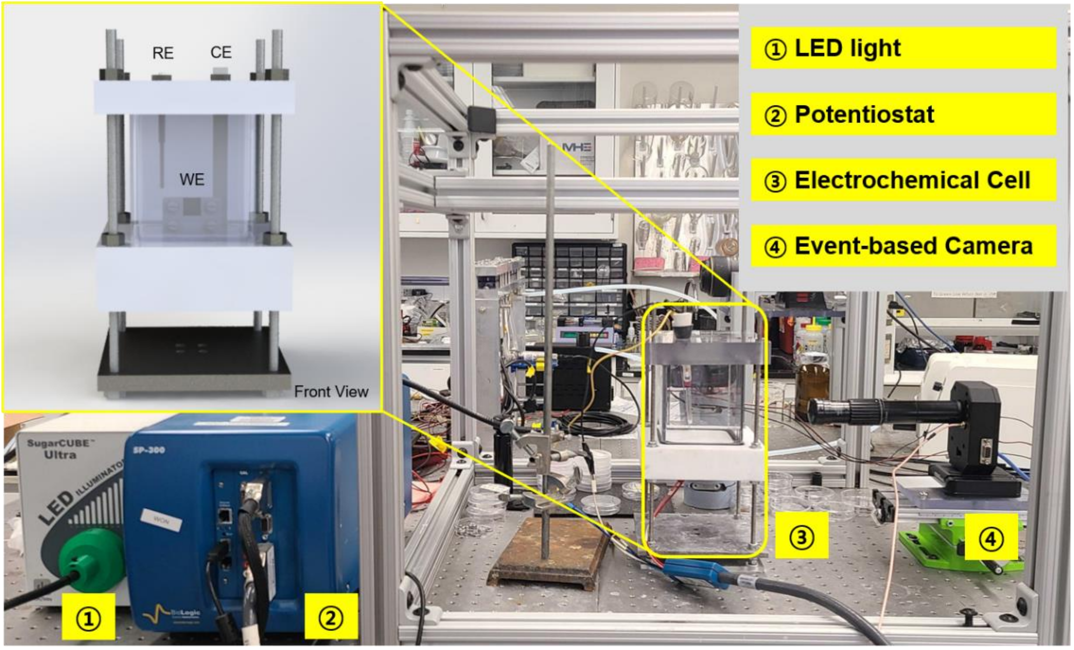

Figure 9. Experimental Setup for Three-Electrode Cell. The main components include a LED light source, a Biologic SP-300 potentiostat, an electrochemical rig, and an event-based camera.

All experiments were performed in a quiescent electrolyte (potassium hydroxide) at room temperature and atmospheric pressure. The electrolyte concentration was 0.2M KOH and 1M KOH, prepared by dissolving KOH pellets (Fisher Chemical) in 300 ml of deionized water. Prior to the experiments, the solution was purged with nitrogen gas for 10-15 minutes to ensure its purity. The reference electrode was a mercury/mercury oxide electrode (EF-1369, BASi Research Products), and the counter electrode was a nickel sheet with a thickness of 1 mm and a purity of 99.96% (MXBAOHENG). The nickel sheet was customized to a dimension of 1cm×8 cm, thereby ensuring sufficient capacity to support high currents, in consideration of the surface area of the working electrode.

2.2 Preparation of Samples

In this study, nickel and copper served as the working electrode. The samples were prepared in the following types: (i) porous nickel foam, (ii) copper plate, and (iii) copper wire. Prior to conducting experiments, all samples underwent a process of sonication in ethanol to remove contaminants and oxide layers on the surface. Subsequently, they were washed in deionized water and dried using an airflow.

(i) Porous Nickel Foam

Porous nickel foam was employed to observe and analyze the behavior of bubbles as they form and move through its porous structure. Commercial porous nickel foam (thickness 1.6mm, porosity 97%, pore size ~0.25mm, 110 PPI, MSE Supplies) was used as the working electrode (WE). The samples were sandwiched between two glass slides to enhance the visualization of bubbles inside the electrodes. They were then securely fastened within a laser-printed acrylic holder using PTFE screws and nuts. The entire assembly was oriented vertically and stabilized with silicone sealant. Additionally, the nickel foam sample was connected to a wire by compressing the holder, and the wire exposed to the electrolyte were shielded by a layer of liquid insulating tape to mitigate current leakage. As shown in Figure 10, the sample's front and back sides were covered with glass slides in order to prevent the formation of bubbles in the gap between the nickel foam sample and the glass slides. This ensured that the observation was solely focused on the bubbles within the porous structure.

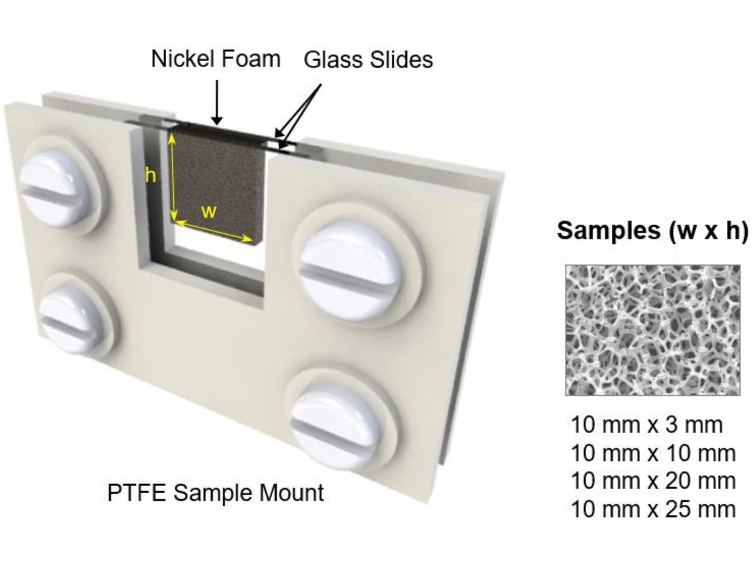

Figure 10. Porous Nickel Foam Sample Mounted in an Acrylic Holder

(ii) Copper Plate

Copper plate was employed as the working electrode to investigate electrochemical gas bubble generation on a flat surface. The copper sample was prepared by cutting copper tape into dimensions of 10 mm x 5 mm x 0.5 mm (width × height × thickness) and polishing it with sandpaper to smooth the rough surface. The sample was vertically placed with an electrode holder (PTFE platinum electrode holder, StonyLab). Epoxy paste was applied around the copper sample to prevent the solution from penetrating into the interspace. Consequently, only the top face of the sample was exposed to the electrolyte, as illustrated in Figure 11, with a surface area of 0.025 cm^2.

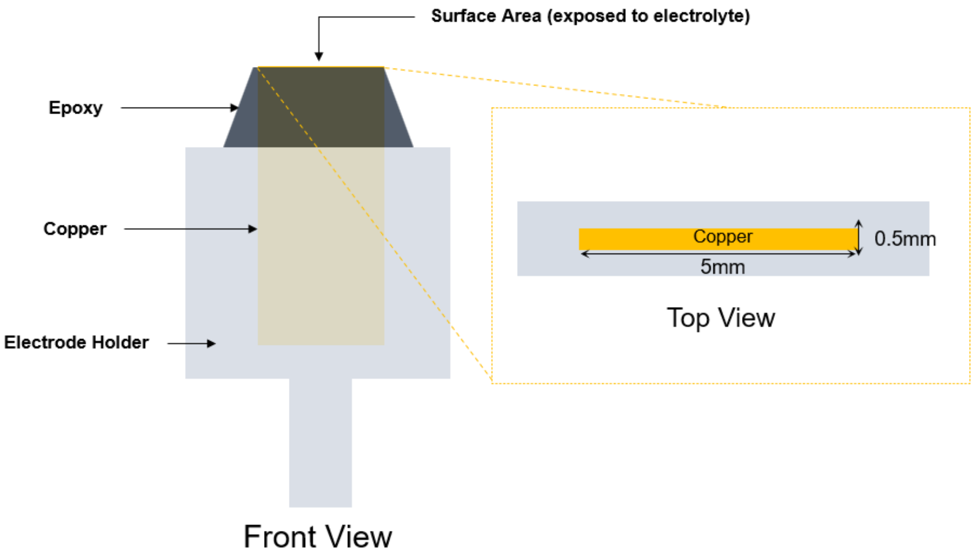

Figure 11. Copper Plate Sample Mounted in an Electrode Holder

(iii) Copper Wire

Copper wire was employed as the working electrode to examine bubble behaviors in the mass transport-dominated regime of high current density. The working sample was prepared utilizing a jump wire. To expose only the top face of the wire as the active surface area, the rest of the wire was covered with epoxy paste. Figure 12A shows a schematic of the sample preparation process. The wire's tip was placed upside-down on a flat surface, and the surrounding area was filled with epoxy. After the epoxy solidified, the exposed surface was polished and cleaned according to the previously mentioned process.

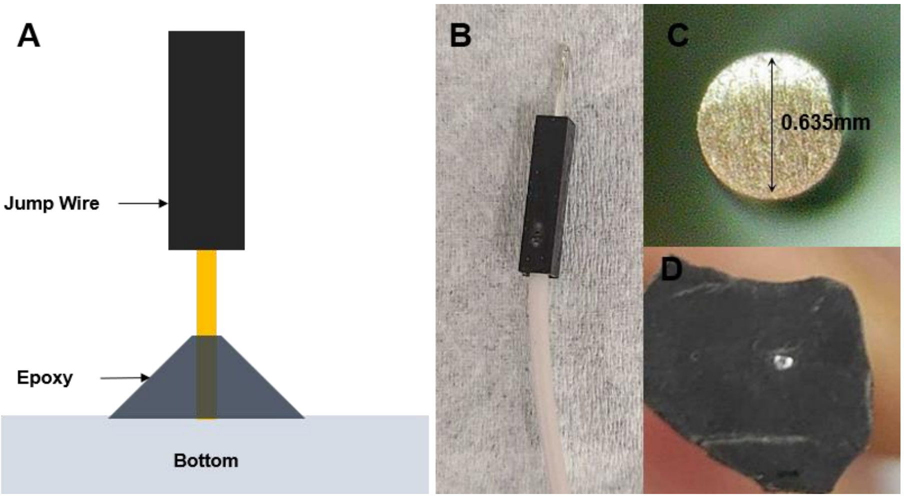

Figure 12. Copper Wire Sample.

A) The copper wire, used as the working electrode, is shown mounted upside-down with its tip in contact with the flat bottom substrate. The surrounding area is filled with epoxy to ensure only the top face of the wire is exposed as the active surface area. B) Photograph of the jump wire. C) Close-up image of the working electrode's surface. The circular area with a diameter of 0.635 mm is the polished and cleaned. D) Image of the electrode's surface

2.3 Electrochemical Experimental Methods

The study of gas bubble generation and its performance impact was mainly conducted by three electrochemical techniques: Cyclic Voltammetry (CV), Linear Sweep Voltammetry (LSV), and Chronoamperometry (CA). The measured potential (vs. Hg/HgO) was converted to the potential versus the reversible hydrogen electrode (RHE) for standardizing electrochemical data. The conversion is achieved by the Nernst equation as follows:

$$E_{RHE} = E_{Hg/HgO} + 0.059 \times pH + E^{o}_{Hg/HgO} \qquad \text{Eq. (16)}$$

where E_{RHE} is the potential versus the reversible hydrogen electrode. $E_{Hg/HgO}$ is the measured potential versus the Hg/HgO reference electrode. $E^{o}_{Hg/HgO}$ is the standard potential of the Hg/HgO reference electrode, which is 0.098V at 25 °C.

The uncompensated solution resistance (R_u) between the WE and the RE was determined using electrochemical impedance spectroscopy (EIS) in a steady state without bubble generation. The range of frequency for the EIS measurement was from 100kHz to 1Hz, with a potential amplitude of 10mV.

2.3.1 Electrochemical Measurement Techniques

Cyclic Voltammetry and Linear Sweep Voltammetry

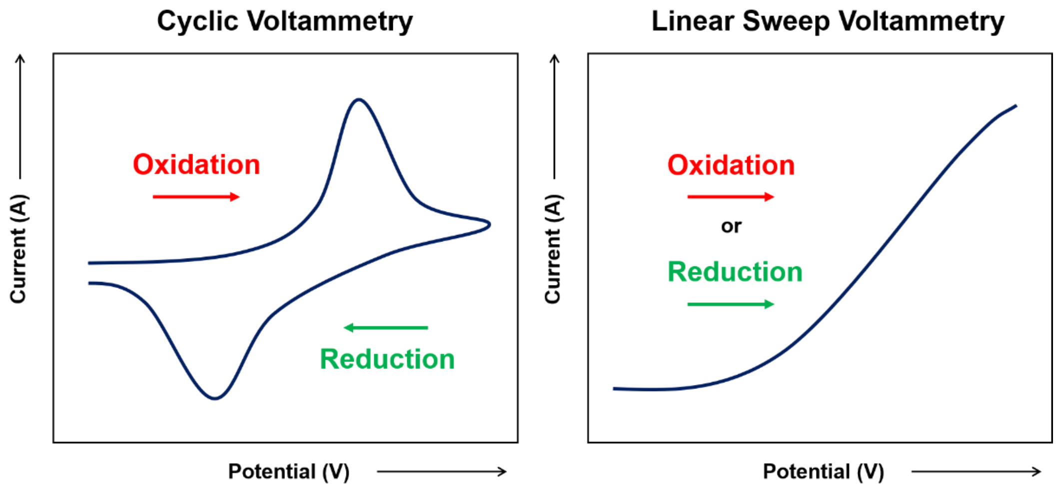

Figure 13. Cyclic Voltammetry and Linear Sweep Voltammetry. Cyclic voltammetry sweeps potential back and forth between two set values, while linear sweep voltammetry sweeps potential in one direction.

Cyclic voltammetry (CV) is an electrochemical technique used to study reduction and oxidation reactions. In CV, the potential of a working electrode is linearly swept back and forth between two set values while measuring the current response, and the resulting current-potential plot is called a voltammogram. Similarly, linear sweep voltammetry (LSV) is a technique to analyze redox behavior, but it involves sweeping the potential linearly in one direction from an initial value to a final value at a constant rate.

In this study, CV was performed as an electrochemical pretreatment by repeatedly scanning the potential until stabilization was achieved. This process activated the electrode surface, ensuring consistent and reliable measurements. Moreover, the CV was used to measure electrochemically active surface area (ECSA) of the working electrode. Linear sweep voltammetry was performed at a scan rate of 50 mV/s in the potential range up to 10V. The LSV measurement was utilized for determining the OER polarization curves. This allowed for the precise measurement of the overpotential and current density associated with the oxygen evolution reaction (OER).

Chronoamperometry

Chronoamperometry (CA) is a technique utilized for examining the kinetics of electrochemical reactions and the diffusion of reactants to the electrode surface. In CA, a constant potential is applied to the working electrode, and the resulting current is measured over time. While LSV focuses on how current changes with varying potential, CA examines current behavior over time at a constant potential, providing insights into reaction stability and mass transport properties.

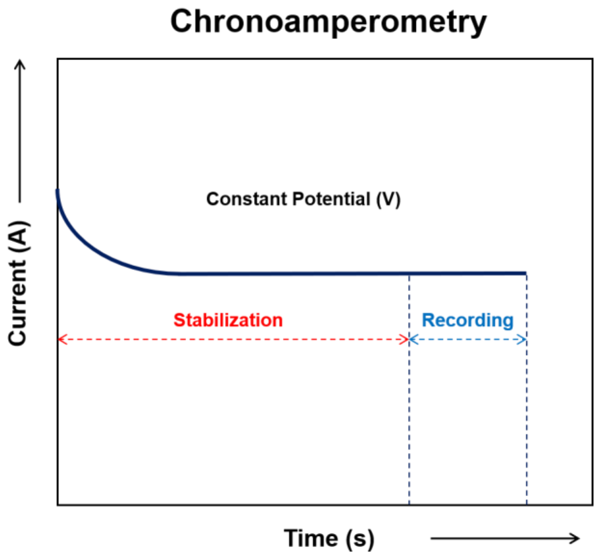

Figure 14. Chronoamperometry. This technique inputs constant potential and examines the current response. A period of stabilization is necessary before data collection

In this study, chronoamperometry (CA) was conducted to observe the impact of bubbles on the current. The resulting current was then correlated with bubble statistics. As depicted in Figure 14, a pretreatment period for stabilization was applied for 120 seconds before recording the current. This process ensured a steady-state condition for accurate and reliable current measurements. According to Faraday's law, bubble generation is proportional to the current. As the current increases, the flux of oxygen bubbles also increases, demonstrating the direct relationship between the electrochemical current and bubble formation.

2.3.2. Current Density and Surface Area

Determining the surface area of an electrode is crucial in electrochemical analysis because it directly impacts the interpretation of overall electrochemical performance. The measured current (i) is normalized by the surface area (A) to calculate the current density (j) [Eq. (17)].

$$Current\ Density\ (j) = \frac{Current\ (i)}{Surface\ Area\ (A)}\ [A/cm^2] \qquad \text{Eq. (17)}$$

For current density normalization, projected area (PA), geometric area (GA), and electrochemically active surface area (ECSA) have all been widely utilized in the literature [38-40]. The projected area refers to the two-dimensional surface area of the electrode. It is calculated by multiplying the width by the length. The geometric area is the three-dimensional surface area of the electrode, calculated by adding up all the areas that come into contact with the electrolyte. However, the geometric area is insufficient because it often overlooks factors such as morphology, particle size and porosity, leading to significant errors [38]. Instead, ECSA can be employed for more accurate normalization. ECSA refers to the surface area of an electrode that actively participates in electrochemical reactions. It is typically determined using the double-layer capacitance (C_{dl}) and the specific capacitance of the electrode material (C_S) with the following equation.

$$ECSA = \frac{C_{dl}}{C_s} \qquad \text{Eq. (18)}$$

$$C_{dl} = \frac{i_a + |i_c|}{2 \cdot \upsilon} \qquad \text{Eq. (19)}$$

The double-layer capacitance (C_{dl}) can be measured experimentally through cyclic voltammetry. Specifically, from a cyclic voltammogram, the double-layer capacitance is obtained using the equation (19), where i_a is the anodic current, i_c is the cathodic current, and υ is the scan rate. However, determining the specific capacitance (C_S) is challenging, which impacts the precise assessment of the ECSA. As a result, it is common practice to use a universal specific capacitance, which is 0.04 mF/cm^2 [39]. Consequently, this method provides a rough estimation of ECSA since the specific capacitance varies between different materials.

In this study, copper plate and wire samples were evaluated based on their projected areas. In contrast, the porous nickel foam was analyzed using both the GA and the ECSA. The complex structure of the porous nickel foam necessitated the use of ECSA to capture a more accurate representation of its active surface, and GA to compare it with the ECSA.

2.4 Visualization and Analysis

Oxygen bubble dynamics was observed using an event-based camera (EVK-3, Prophesee) equipped with a microscope lens (Magnification 0-4x, InfiniProbe-MS, INFINITY). The camera had a resolution of 1280 x 720 pixels (pixel size 4.86 x 4.86 um) and was positioned 3cm from the sample. To provide backlighting for the sample, a LED light source (SugarCUBE LED Illuminator, Edmund) was used. The synchronization between the visualization and electrochemical data was achieved using a BNC to SMA trigger cable, allowing for the examination of bubble impact on the electrolysis process [Appendix A].

(i) Event-based Camera

An event-based camera, also known as a neuromorphic camera, is a specialized type of camera that mimics the way biological retina processes visual information. The event-based camera captures changes in brightness at the pixel level within a scene, as opposed to conventional cameras recording multiple frames at a predetermined frame rate. Each pixel in the event-based imaging sensor operates independently and has thresholds for triggering events [41]. An increase in intensity of light beyond the threshold generates an ON event, while a decrease in intensity triggers an OFF event. Each event contains data including a coordinate, polarity (ON or OFF), and a timestamp. Generated events can be visualized during post processing, by accumulating the events and reconstructing frames.

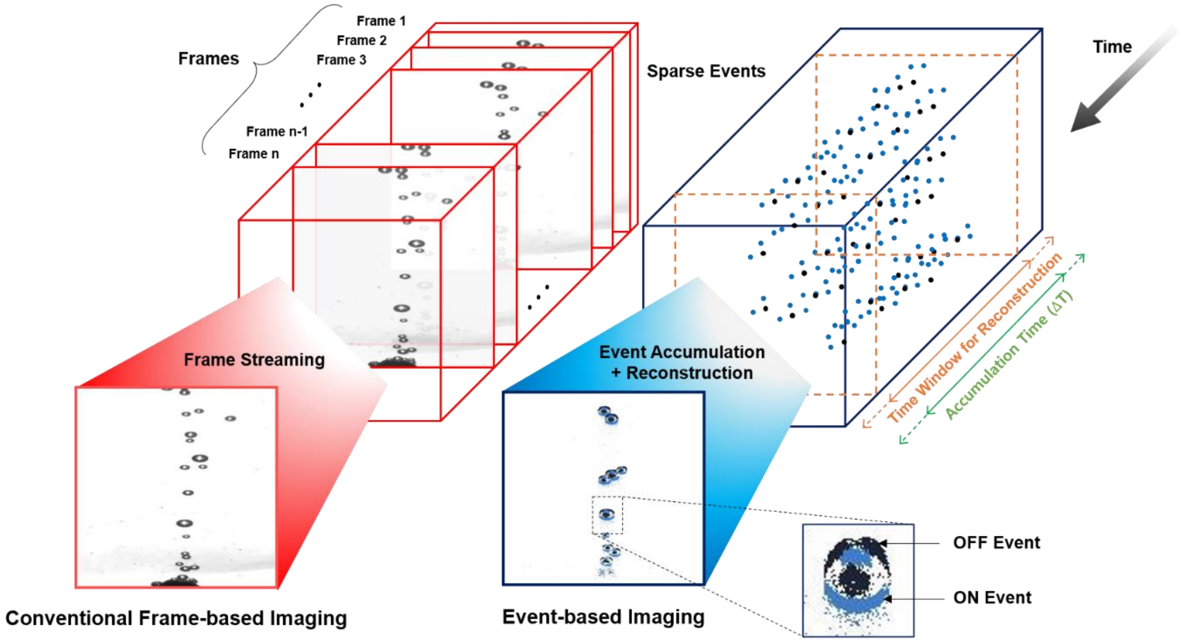

Figure 15. Comparison of Conventional and Event-Based Imaging Techniques. The left image depicts how conventional frame-based cameras work, processing multiple frames taken over pre-set time period. In contrast, the right image depicts the operation of event-based cameras, which capture individual events asynchronously. Blue dots indicate ON events, and black dots represent OFF events.

Figure 15 illustrates the comparison between conventional frame-based imaging and event-based imaging. In the conventional method, entire scenes in the frames are captured at regular intervals, resulting in large data volumes and potential redundancy. In contrast, event-based imaging only records changes asynchronously at the pixel level, and then accumulates events over a specified time window (ΔT), and uses these events to reconstruct visual representations. This method significantly reduces redundant data and enhances temporal resolution, allowing for event-based cameras to operate with very low latency, high dynamic range, and efficient data processing [42].

Figure 16 highlights how different threshold (contrast detection) settings in event-based imaging impact event generation and visualization. Lower thresholds result in more dense event data, sensitively capturing finer changes in the scene, while higher thresholds result in sparser data, focusing on more significant changes. It is essential to adjust the threshold according to the lighting conditions and the application requirements. Additionally, setting appropriate accumulation time and time window for frame generation is crucial to ensures optimal event visualization. This study utilized event-based imaging to analyze bubble dynamics in the water electrolysis process, examining the phenomenon visually and statistically. For all the samples, a quantitative investigation was performed using analytic algorithms. Particularly, using porous nickel foam, active sites of bubble formation and pathways within the porous structure were identified by leveraging the ability to capture solely moving objects within the scene.

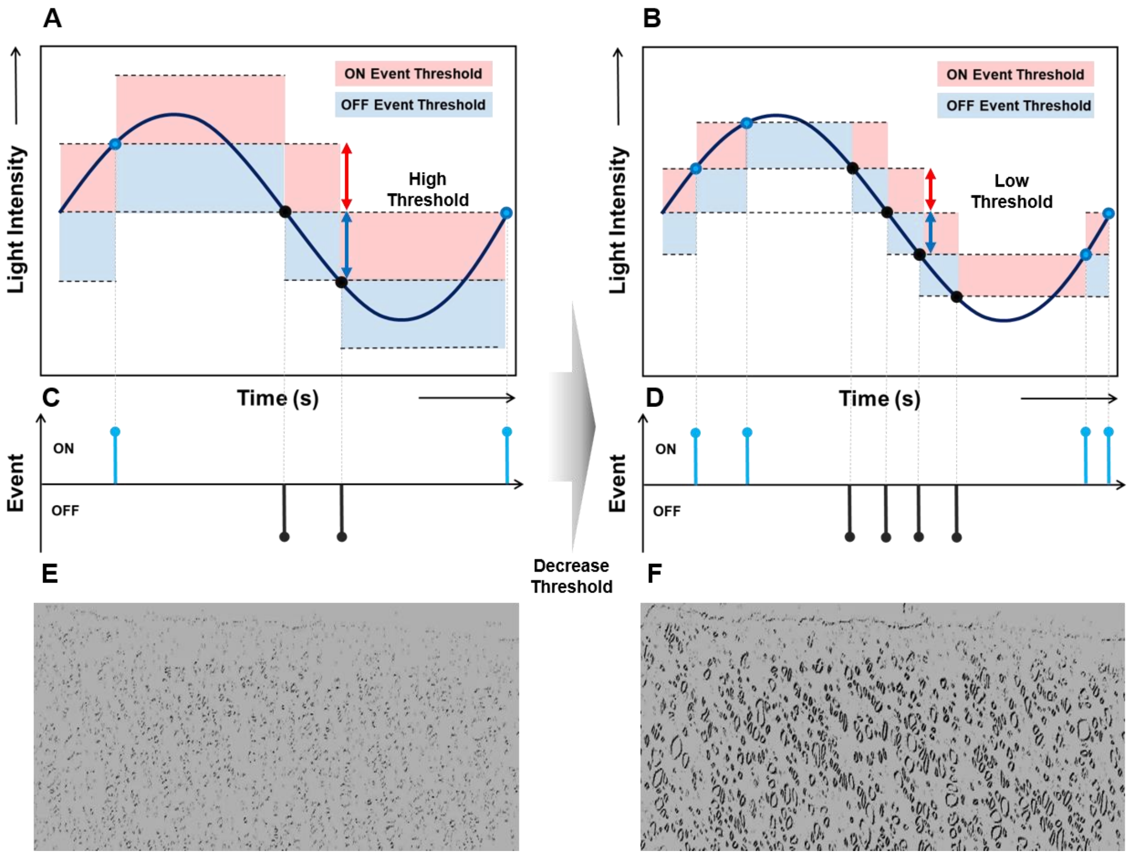

Figure 16. Impact of Threshold Setting on Event Detection and Visualization [43]**.** (A) and (B) compare how different threshold settings work in capturing events. (A) has a higher threshold than (B). The red areas represent the thresholds set for detecting ON events, which occur when the light intensity increases above a certain level. The blue areas indicate the thresholds for detecting OFF events, triggered when the light intensity decreases below a set point. (C) and (D) represent generated events by different threshold setting from (A) and (B), respectively. (E) and (F) display example images (porous foam) that can be produced from different threshold settings. Adjustable thresholds generally include contrast sensitivity, bandwidth biases, and refractory periods. Contrast sensitivity controls the contrast threshold for generating ON and OFF events. Bandwidth biases determine the rate of illumination changes that can be filtered out. Refractory periods influence the blind time after event generation.

(ii) Feature Extraction

Prophesee's Metavision SDK includes advanced analytic algorithms that enable the extraction and analysis of various features from event data. The features extracted include the number of bubbles and bubble departure size [Appendix B]. In this study, the number of events, determined by counting the total events generated by bubbles, offered a measure of the overall activity level in the scene, particularly in relation to bubble formation and movement. Bubble counts were essential for examining the frequency of bubble release from the electrode surface and monitoring changes in the bubble population over time, while analyzing bubble size helped in understanding bubble growth rates and the distribution of bubble sizes across different current density levels. Each of these features contributed to a comprehensive understanding of bubble dynamics in the electrolysis process.

Chapter 3: Results and Discussion

This chapter details the experimental findings for three electrode types: porous nickel foam, copper plate, and copper wire. The investigation focused on the bubble dynamics of these electrodes during the oxygen evolution reaction (OER), utilizing electrochemical measurements and quantitative analysis. All experiments were conducted in a 0.2 M KOH solution. Polarization curves were acquired via linear sweep voltammetry, conducted at a scan rate of 50 mV/s within a potential range of 0 to 1 0 V. The duration of each linear sweep voltammetry was approximately 180 seconds. Potentials were referenced against the reversible hydrogen electrode (RHE). The solution resistance between the reference and working electrodes was determined using electrochemical impedance spectroscopy (EIS). The EIS measurements spanned a frequency range from 200 kHz to 1 Hz, with a potential amplitude of 10 mV.

3.1 Porous Nickel Foam

Porous nickel foam was fabricated in four different dimensions, each with a consistent width of 10 mm and varying heights: 10 mm × 3 mm, 10 mm × 10 mm, 10 mm × 20 mm, and 10 mm × 25 mm. These are labeled as h3, h10, h20, and h25, respectively.

Determination of Electrochemically Active Surface Area

The electrochemically active surface area (ECSA) of these samples was determined by dividing the double-layer capacitance (C_{dl}) by the specific capacitance (C_s, 40 μFcm^{-2}). To assess the double layer capacitance, cyclic voltammetry (CV) was performed at various scan rates, ranging from 2 to 12 mV/s. The measurement window was set to 100mV, centered around the open circuit voltage.

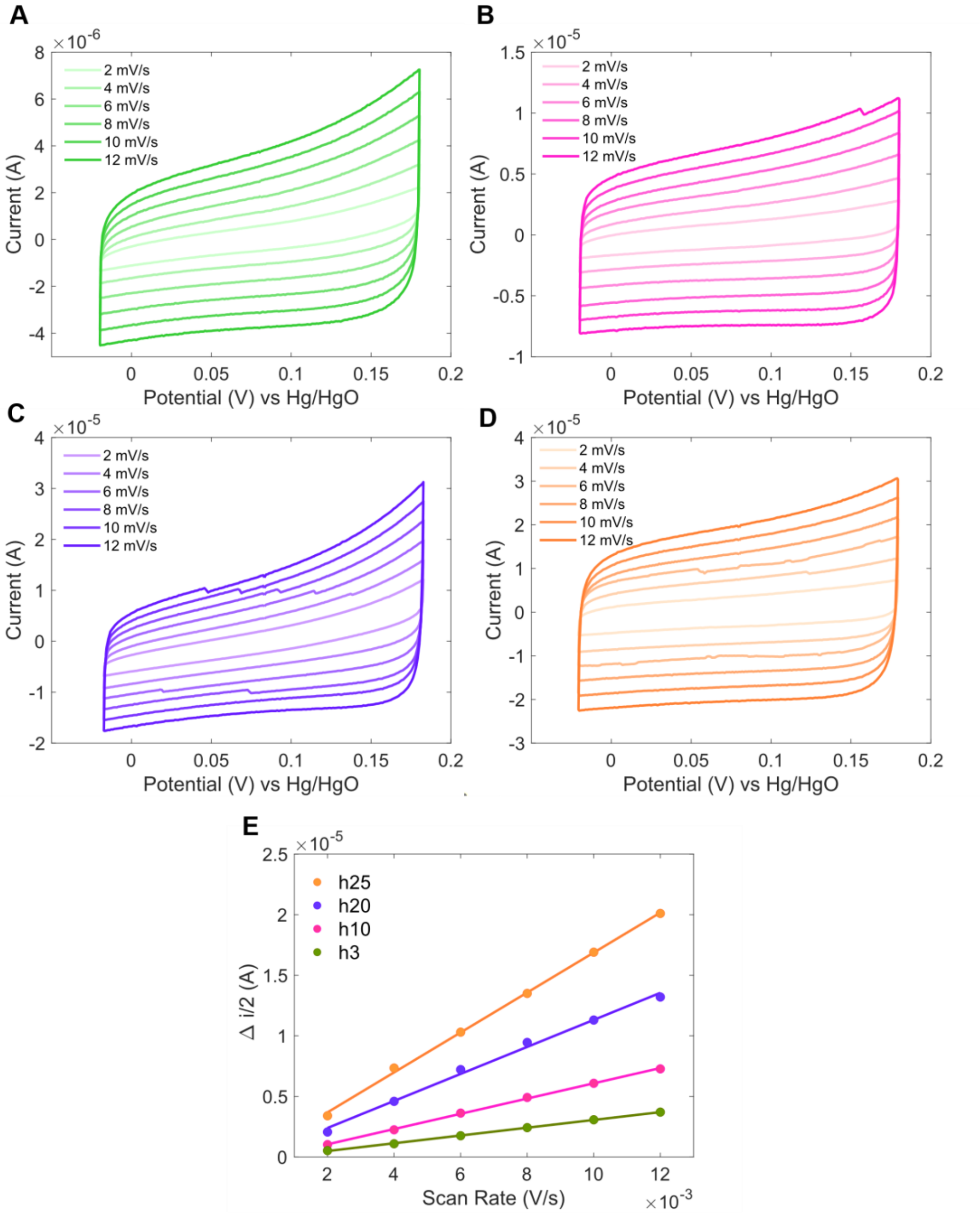

Figure 17. Experimental Results for Determination of ECSA

(A~D) Cyclic voltammograms of h3, h10, h20, and h25, respectively (E) Average capacitive current against the scan rate showing the double layer capacitance.

Table 2: Surface Area and Double-layer Capacitance

	10 mm x 3 mm	**10 mm x 10 mm**	**10 mm x 20 mm**	**10 mm x 25 mm**
ECSA (cm^2)	8.02	15.73	27.9	41.3
C_{dl} (mF)	0.1	0.629	1.12	1.65
Geometric Area (cm^2)	1.02	2.64	4.96	6.12
Ratio (ECSA/GA)	7.86	5.96	5.63	6.75

Figure 17 presents the cyclic voltammetry results used to evaluate the double-layer capacitance, and Table 2 provides a comprehensive summary of the measured ECSA along with the geometric area (GA), the ratio of ECSA to GA, and the double-layer capacitance (C_{dl}). Notably, while ECSA increases with the geometric area, the ratio of ECSA to GA varies across different dimensions. This variation can be attributed to mass transport limitations and infiltration issues. As the size of the samples increases, the infiltration of the electrolyte into the porous structure becomes less efficient, leading to incomplete wetting and limited access to internal surface areas. This incomplete infiltration restricts the available surface for ions charging and discharging, particularly in larger samples where longer diffusion paths and uneven electrolyte distribution aggravates these limitations. Furthermore, the cell configuration, which includes glass slides on both sides, further intensifies these challenges.

Electrochemical Investigation

Figure 18A shows the anodic polarization curves for the h3 to h25 electrodes, while Figure 18B depicts the overpotential as a function of the current density. The overpotential curve was corrected for iR drop to account for the solution resistance between the WE and the RE.

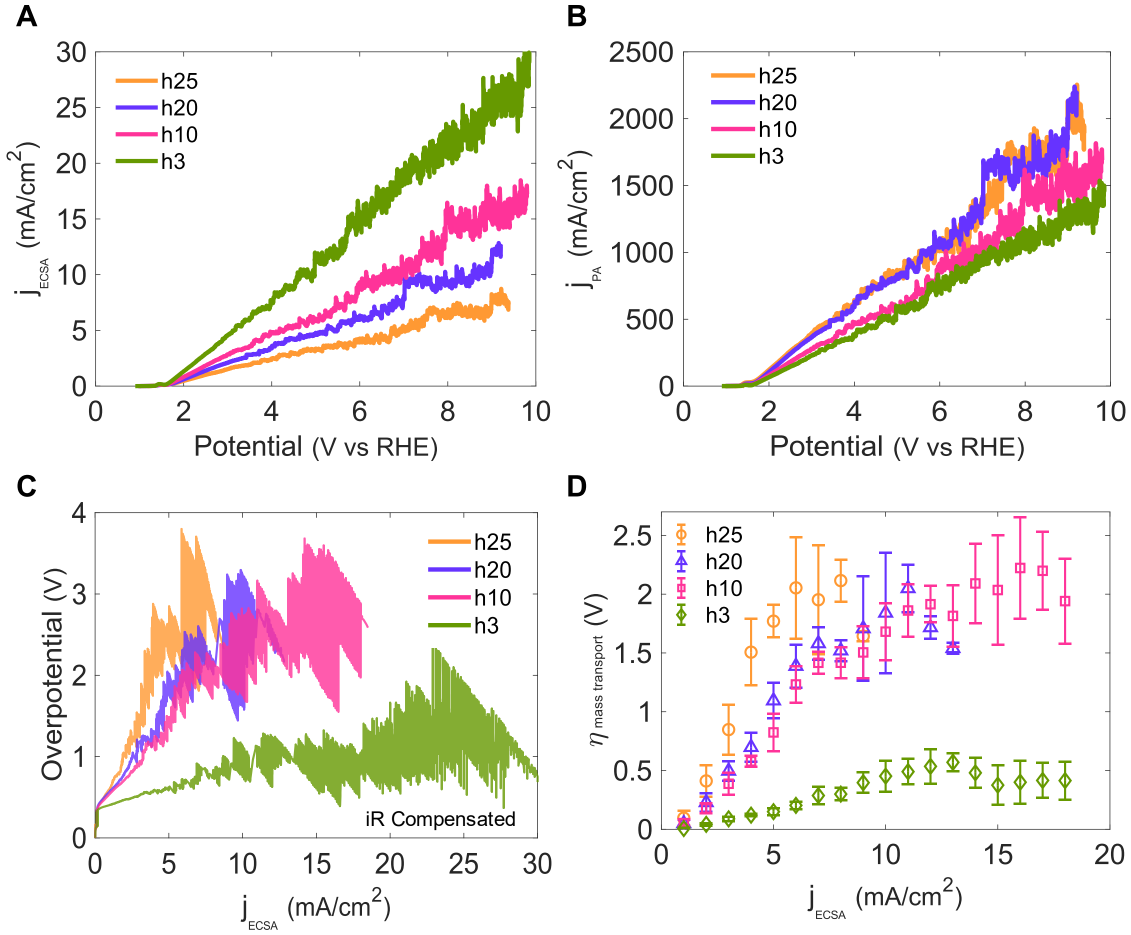

Figure 18. Electrochemical Performance of h3 h10, h20, and h25 Electrodes

(A) Current density (normalized by ECSA) versus potential. (B) Current density (normalized by projected area) versus potential. (C) Overpotential against the ECSA-normalized current density after iR compensation. (D) Mass transport overpotential against the ECSA-normalized current density

The resistances measured via electrochemical impedance spectroscopy (EIS) were 32.5 Ω for h3, 20.1 Ω for h10, 16.1 Ω for h20, and 15.7 Ω for h25. The high resistance values are likely influenced by artifacts inherent to the cell design, in addition to the solution resistance. In the polarization curve, the h3 electrode demonstrated the highest current density with the lowest overpotential. The trend shows that overpotential increases with an increase in sample size. To examine mass transport limitations across different samples, the mass transport overpotential was determined by subtracting the activation overpotential from the iR-compensated overpotential. The activation overpotential was estimated using Tafel fitting, where a linear plot was fitted to the overpotential versus logarithmic current density [Appendix C]. The results are summarized in Table 3 below.

Table 3: Results of Tafel Fitting

	10 mm x 3 mm	**10 mm x 10 mm**	**10 mm x 20 mm**	**10 mm x 25 mm**
Slope (mV dec^{-1})	76.4	162.6	182.4	220.6
η_{10mA/cm^2} **(mV)**	477.3	654.3	709.6	752.6
η_{100mA/cm^2} **(mV)**	553.7	816.9	892	973.2

Figure 18C illustrates that mass transport limitations are most pronounced in the h25 electrode, which exhibits the highest mass transport overpotential. At the initial stages of the reaction, the mass transport overpotential for all samples is negligible due to minor bubble impacts. However, as the reaction progresses into the regime characterized by the vigorous generation of bubbles, the mass transport overpotential increases significantly.

Oxygen Bubble Behavior

The study of bubble dynamics during the oxygen evolution reaction (OER) was conducted using an event-based camera and analytic algorithms of Metavision SDK (Prophesee). The event-based imaging technology enabled quick and efficient analysis of bubble behavior over long measurement periods, reducing the need for extensive data processing commonly associated with high-speed cameras. The analysis focused on bubble departure diameter, release frequency, and nucleation sites in porous nickel foams.

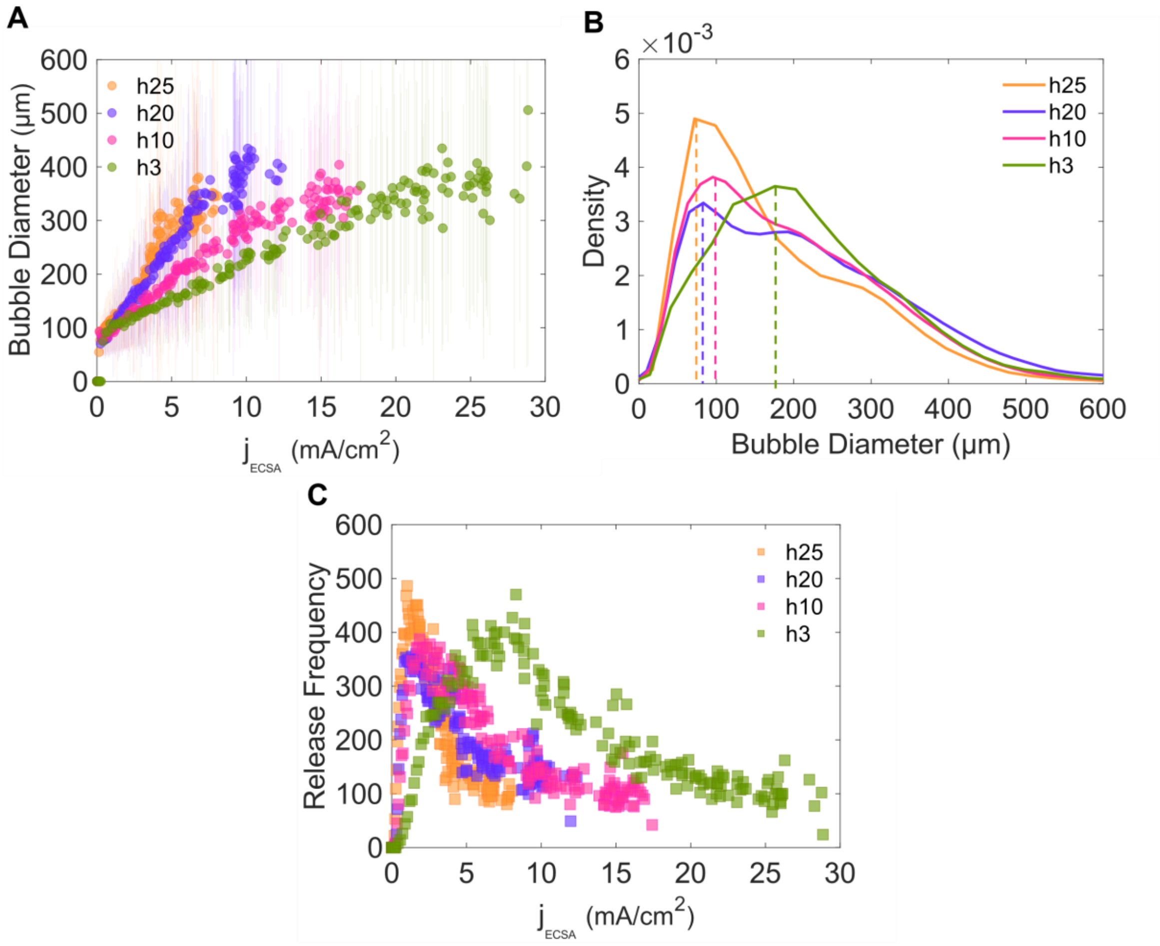

Figure 19. Analysis of Bubble Dynamics during Oxygen Evolution Reactions. (A) Bubble diameter as a function of current density. (B) Kernel density estimation of bubble diameter distributions. (C) Variation of bubble release frequency with current density.

The number of bubbles examined during the LSV measurements were 34,057 for h3, 31,722 for h10, 30,924 for h20, and 34,773 for h25. Figure 19A shows the relationship between the current density and the average bubble diameter for the four electrodes. The data suggests a linear relationship between the current density and bubble departure diameter across all samples. Notably, larger electrodes, such as h25, exhibit a more rapid increase in bubble size as the current density rises. Figure 19B displays the probability density distribution of bubble diameters throughout the entire LSV measurement period. The distribution curves reveal that the most frequent bubble diameter shifts depending on the electrodes. The peaks, indicated by dashed lines, occur at 175.7 μm for h3, 95.4 μm for h10, 83.2 μm for h20, and 71.9 μm for h25. The average bubble diameters for each electrode are 231.3 μm, 206.4 μm, 232.4 μm, and, 186.8 μm, respectively. This trend in bubble size can be attributed to the higher current densities typically observed with smaller electrodes. However, when the current density range is narrowed to 0–8 mA/cm^2 for comparison within the same current density range, the average diameters for h3 to h25 are 150.5 μm, 164.6 μm, 196.4 μm, and 186.8 μm, respectively. This suggest that, under the same current density, larger bubbles tend to form as the electrode size increases. This phenomenon may be influenced by an increase in local current density caused by mass transport limitations. Stronger electric field and localized current density can enhance electrostatic forces, leading to the production of larger bubbles. Figure 19C illustrates the bubble release frequency as a function of current density. Initially, all electrodes exhibit high release frequencies at lower current densities, which rapidly decline as current density increases, indicating a transition to less frequent bubble release. Especially, the h3 electrode shows a delayed drop in frequency, indicating more effective and continuous gas removal. These observations imply that the h3 electrode's stable bubble dynamics may contributed to more efficient oxygen evolution by mitigating bubble-induced mass transport limitations.

Event-based Imaging for Identifying and Visualizing Active Reaction Sites

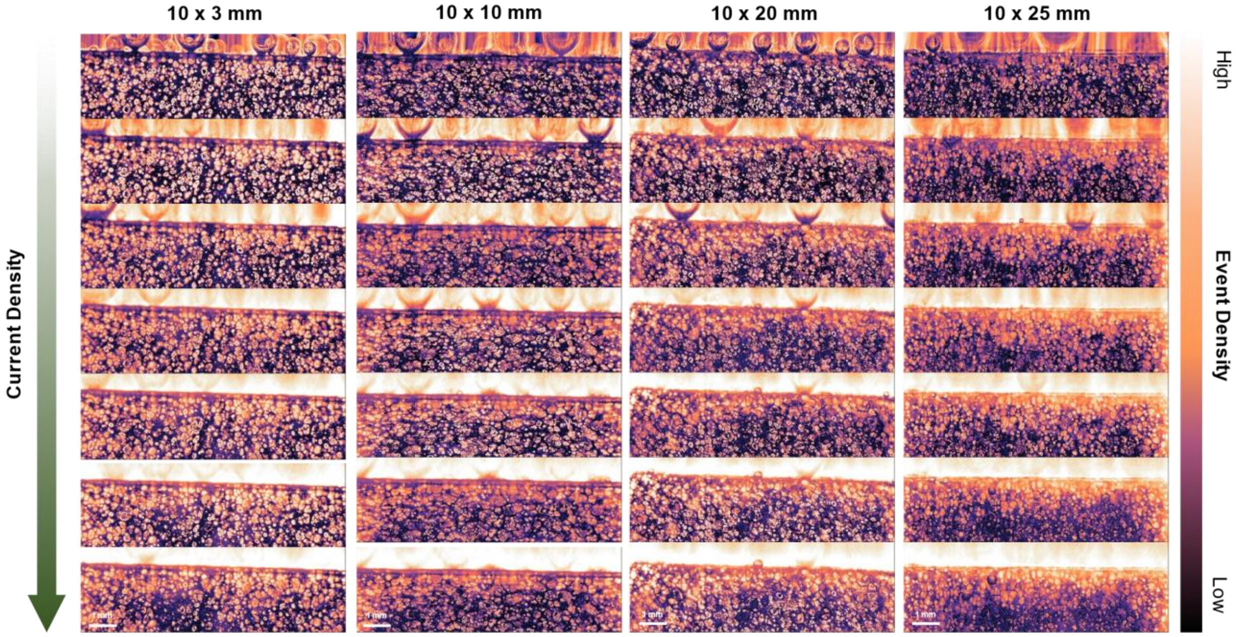

Figure 20. Event-based Images of Nickel Foams during LSV Measurement. Viewing window is 10 mm x 3 mm for all samples. Each column represents event visualizations from four electrodes (h3, h10, h20, and h25), while the rows display the progression of the reaction. The images are color-coded to highlight areas of activity, with colors ranging from dark purple (low activity) to bright orange (high activity).

Event-based imaging provides a powerful tool for visualizing and understanding electrochemical reactions in porous nickel foams. This technique, which captures pixels exclusively of moving elements within the scenes, is particularly adept at focusing on the nucleation and movement of bubbles. By aggregating the events generated over the recording period, it effectively highlights the active reaction sites during the process.

Consequently, this approach facilitates a profound understanding of bubble dynamics and identifies potential areas for optimization within the porous structure.

The images in Figure 20 highlight active areas of event generation caused by bubbles, which can be interpreted as reaction hotspots. The h3 electrode demonstrates a well-distributed pattern of event generation throughout its structure, whereas larger electrodes exhibit more inactive sites in the central area, indicated by a dark purple color. This implies that the electrolyte was unable to effectively penetrate into the deeper surfaces of these larger electrodes, leading to a decrease in gas bubble production within the structure. The limited activity in the central areas indicates potential issues with mass transport, where the lack of electrolyte infiltration results in reduced surface area utilization. This can hinder the reaction efficiency and overall electrode performance, as less active material is participating in the reaction. This observation also explains the phenomenon of larger departing bubbles in the larger electrodes, as depicted in Figure 19A. Due to the restricted mass transport, an uneven distribution of current density arises, resulting in particularly high local current densities at the interface between the electrolyte and the electrode. Furthermore, the analysis proves that event-based imaging can be an effective diagnostic tool to identify areas where the surface is deactivated or where reaction conditions are not ideal. This capability helps diagnose and address issues that reduce efficiency, thus improving overall electrode performance by highlighting regions that need optimization.

3.2 Flat Copper Electrode

Two types of copper electrodes were investigated: a copper plate and a copper wire. This section presents the results for the copper plate. The result for the copper wire can be found in Appendix D

Electrochemical Investigation

For the linear sweep voltammetry (LSV) measurement, a copper plate sample was mounted in an electrode holder, exposing a surface area of 0.025 cm^2 in 0.2 M KOH. Figure 21A presents the polarization curve before iR compensation. The curve exhibits a slight variation in slope around 5 V, followed by a continuous increase up to 10 V. Figure 21B shows the overpotential as a function of current density after iR compensation. The solution resistance measured through EIS was 34.1 Ω. The overpotential curve reveals a more distinct variation. Figure 21C displays the Tafel plot of overpotential versus the logarithm of current density. The Tafel fitting was applied only in the linear region between approximately 1.5 mA/cm^2 and 2.5 mA/cm^2 of logarithmic current density. In the Figure 21B and 21C, three distinct stages are identified based on variations in overpotential. In Region ①, the reaction kinetics align with the Tafel plot. Region ② begins when the overpotential deviates from the Tafel plot, suggesting the onset of mass transport limitations. In Region ③, the overpotential exhibits a sharp increase.

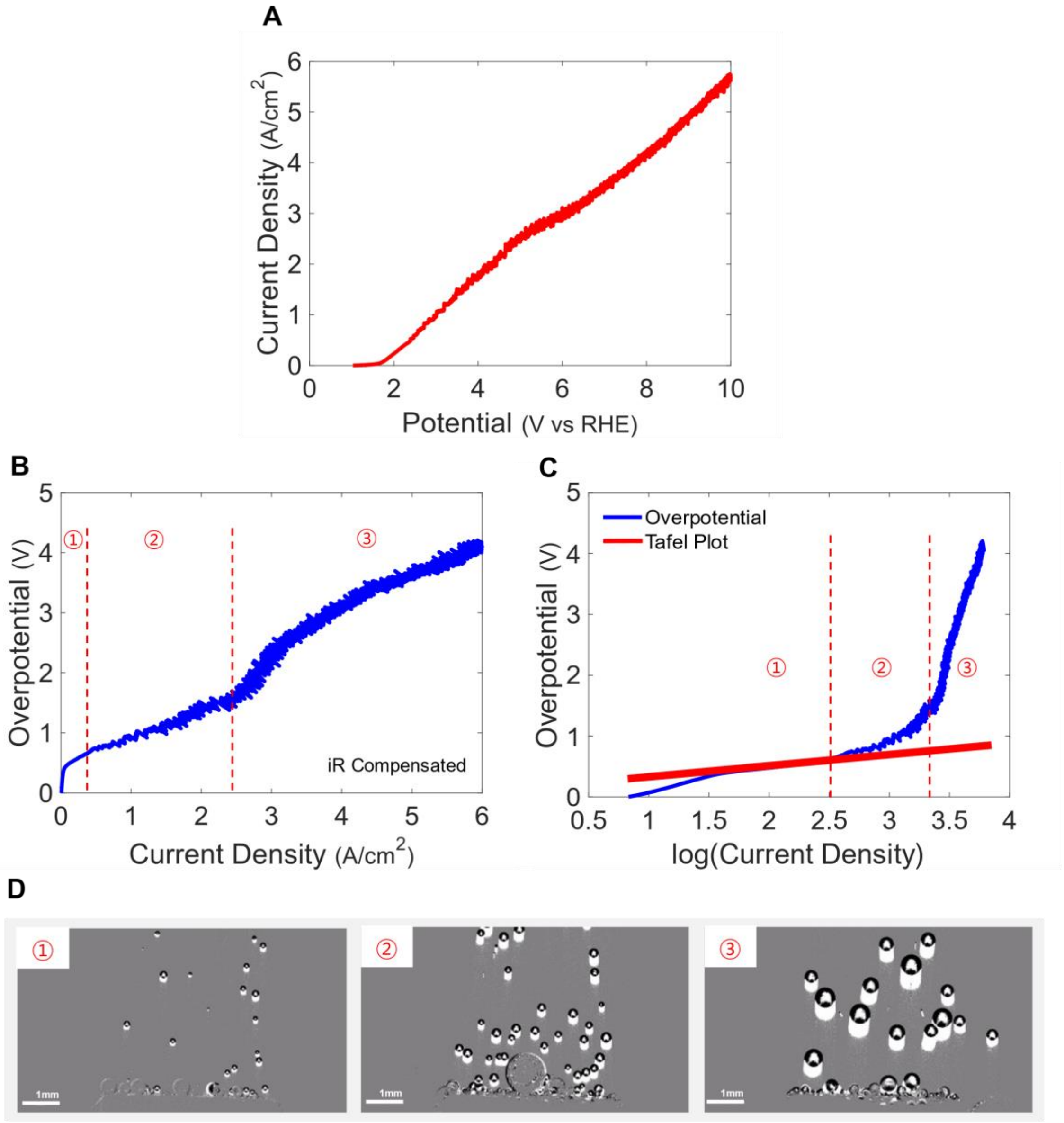

Figure 21. Electrochemical Characterization of a Flat Copper Electrode

(A) Polarization curve. The potential measured was converted to the potential relative to the reversible hydrogen electrode, without iR compensation. (B) Overpotential as a function of current density (A/cm^2) with iR compensation. (C) Tafel plot to the overpotential versus logarithmic current density (mA/cm^2). The Tafel fitting was conducted beyond logarithmic current density of 1.5, where the data exhibited a linear region. (D) Event-based Images taken during the regions of ①, ②, and ③

Images in Figure 21D correspond to the three distinct regions identified in Figures 21B and 21C. Image ① illustrates the initial stage with sparsely distributed, small bubbles. Image ② shows an intermediate stage with increased bubble formation, suggesting higher reaction activity. Image ③ reveals denser and larger bubble formation, indicating significant reaction activity and potential mass transport limitations. Hence, the slope change around 5 V suggests a shift in the reaction mechanism caused by bubble formation. In addition, the transition from sparse to dense bubble formation highlights an increasing electrochemical reaction rate and indicates the possible onset of mass transport limitations.

Overpotential Analysis

Figure 22 shows the remainder overpotentials: activation, ohmic, and mass transport overpotential. The activation overpotential was calculated using the Tafel equation, $\eta_{act} = 187.4 + 170.8 \log j$, which was derived through the Tafel fitting in Figure 21C. The ohmic overpotential was obtained by multiplying the current by the solution resistance. The mass transport overpotential was then calculated by subtracting both the activation overpotential and the ohmic overpotential from the total overpotential.

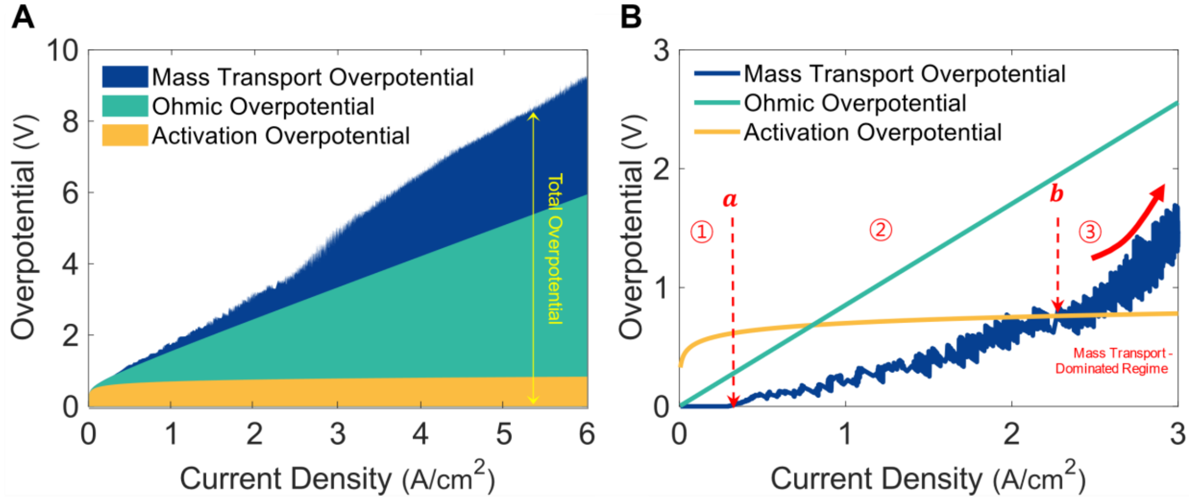

Figure 22. Overpotential Analysis of a Flat Copper Electrode.
(A) Remainder overpotentials as a function of current density: activation overpotential, ohmic overpotential, and mass transport overpotential. (B) Transition toward mass transport-dominated regime.

Figure 22B presents a detailed analysis in the range up to 3 A/cm^2. The label ***a*** denotes the onset of mass transport limitation around 0.3 A/cm^2, which begins to impact the electrolysis performance. The label ***b*** indicates the point where the mass transport overpotential exceeds the activation overpotential at 2.4 A/cm^2. Prior to 0.3 A/cm^2, the activation overpotential is the predominant factor. However, as the reaction continues, the ohmic overpotential becomes outstanding. Notably, a significant increase in mass transport overpotential is observed around 2.4 A/cm^2 with substantial fluctuations. This phenomenon demonstrates a transition to a mass transport-dominated regime.

Oxygen Bubble Behavior

A comprehensive analysis of bubble dynamics at a flat copper electrode is presented in Figure 23. Figure 23A shows the release frequency of bubbles in Hertz, separated by regions ①, ②, and ③. The release frequency gradually rises up to the region ②, and it exhibits a sharp drop around 2.4 A/cm^2 and a stabilized frequency, approximately 100 Hz, in the mass transport-dominated regime (③). Figure 23B depicts the average bubble diameter against the current density. The variation in slope is observed in the transition from the Region ① to ②. Afterward, it shows the consistent growth rate. Considering the findings shown in Figure 23A and 23B, it can be inferred that the reduction in release frequency could contribute to limited mass transport. This limitation arises as the bubble size enlarges and the release frequency declines, which hampers the efficient transport of reactants and products. Figure 23C presents a comparison between experimentally measured diameters and those predicted using the ideal gas law [44] [Appendix E]. The close agreement of these values validates the reliability of the event-based imaging method. Figure 23D shows a kernel density estimation for bubble diameter distribution depending on the three regions. The result reveals that as the reaction moves to the mass transport-dominated regime, the bubble size grows and its distribution becomes bimodal. The bimodal distribution can be attributable to the active coalescence of bubbles at higher current densities. Consequently, this comprehensive analysis of bubble behaviors underscores the importance of controlling bubble dynamics to improve the efficiency of electrochemical reactions.

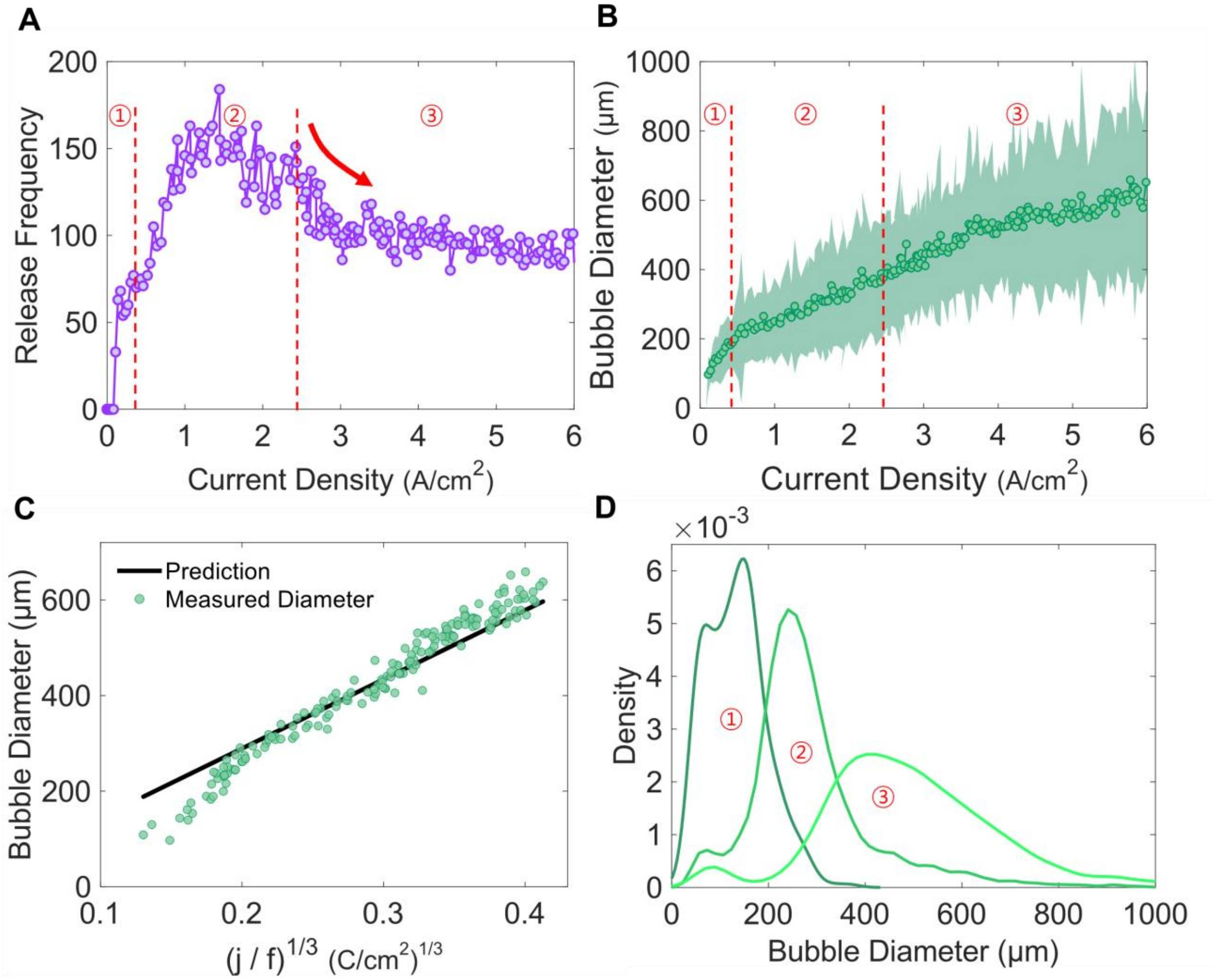

Figure 23. Analysis of Bubble Dynamics at a Flat Copper Electrode.

(A) Variation of bubble release frequency with current density. (B) Bubble diameter as a function of current density. (C) Comparison of measured and predicted bubble diameter [Appendix E]. (D) Kernel density estimation of bubble diameter distributions

Fluctuation Analysis

Current density is subject to fluctuation as the electrochemical reaction advances towards a mass transport-dominated regime. The main cause of the fluctuation has been identified as the production of bubbles. Fluctuations during electrolysis process can have an adverse impact on catalyst stability and electrolysis efficiency. To better understand the bubble impact on the fluctuation, Fast Fourier Transform (FFT) was utilized. Figure 24A displays a scatter plot of all recorded bubble diameters throughout the entire LSV measurement period. These data are then plotted for visualizing the fluctuation as shown in Figure 24B. The plots are segmented into three regions, corresponding to the previous categories. Figure 24C represents the fluctuation of mass transport overpotential over the same period. Both the bubble diameter and the mass transport overpotential were examined using Fast Fourier Transform (FFT) as shown in Figure 24D. The dominant frequencies, marked in the plots, indicate the key frequencies at which the most significant dynamic behaviors occur. The comparison between bubble dynamics (green) and mass transport overpotential (blue) shows how these two factors interact and influence each other at different stages of the electrochemical process. The shift in dominant frequencies from region ② to ③ reflects the changing dynamics as the system transitions to being more influenced by mass transport limitations. Consequently, this analysis implies a notable correlation between bubble dynamics and mass transport.

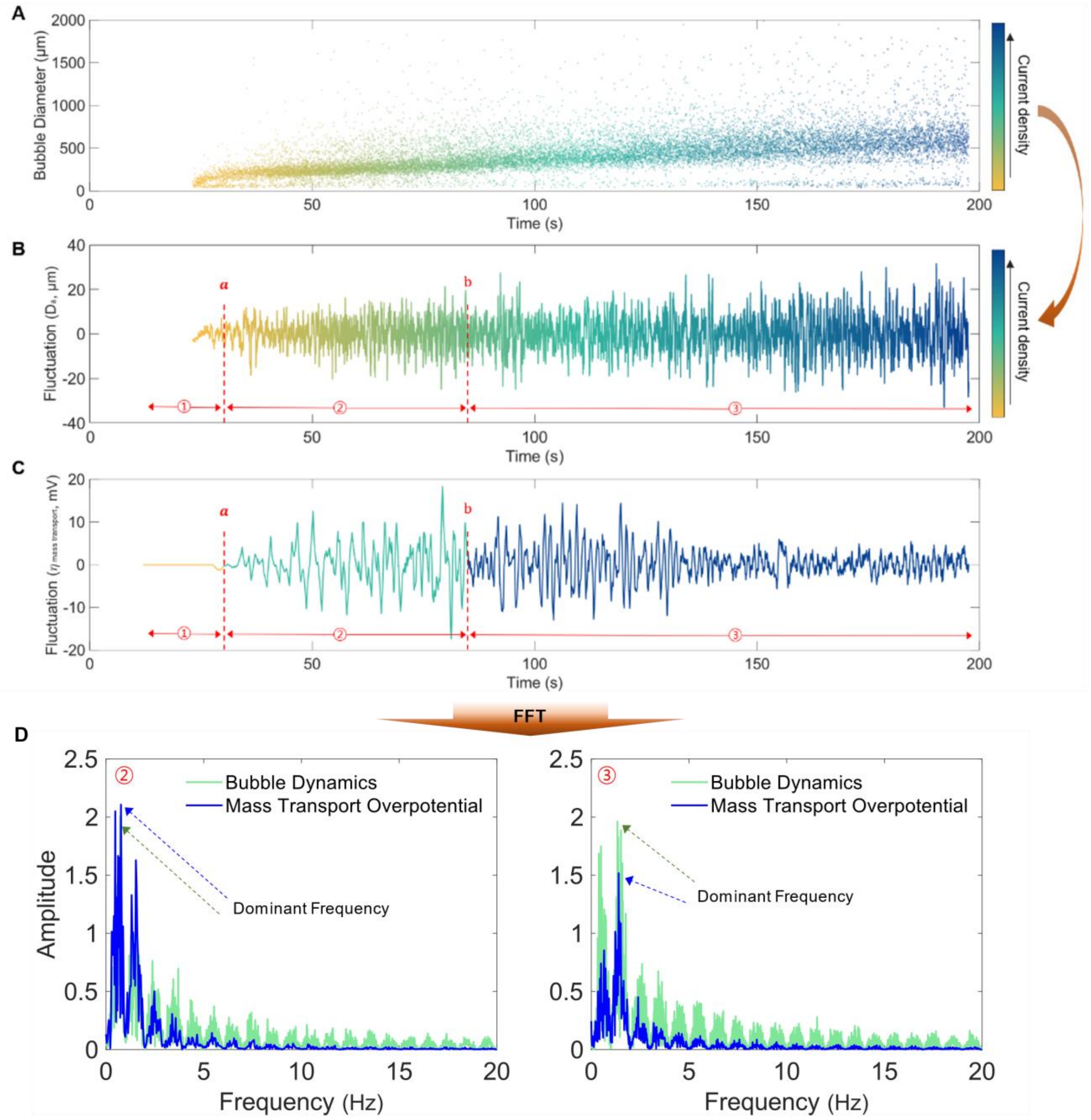

Figure 24. Frequency Analysis of Bubble Dynamics and Overpotential.

(A) Temporal evolution of bubble diameter. (B) Fluctuations in bubble diameter over time. (C) Fluctuations in mass transport overpotential over time. (D) Frequency domain analysis: bubble dynamics vs. mass transport overpotential.

Chapter 4: Conclusion

This research provides an in-depth analysis of bubble generation and its impact on performance during water electrolysis process. For this study, we have explored two types of electrodes: porous nickel foams and flat copper, and have utilized an event-based imaging technique to gain insights into the underlying processes.

Summary of Findings

First, event-based imaging technique has proven to be a highly effective tool for studying the dynamics of bubble generation. Its ability to operate with high temporal resolution and efficient data processing enabled precise detection and detailed visualization of vigorous bubble activities. Furthermore, the ability to capture solely moving objects not only made it possible to identify reaction hotspots in porous media, but also suggested the potential for diagnosing issues associated with surface defects and catalyst activities in porous media.

Next, the study identified distinct bubble behaviors according to different overpotential regions, and their relationship with limited mass transport phenomena. A rapid drop in bubble release frequency is closely related to the transition to a mass transport-dominated regime, possibly caused by intense coalescence at high current densities.

Finally, the investigation of bubble formation in porous nickel foams revealed that limited mass transport may lead to an increase in local current density, which is related to an increase in bubble size and early drop in release frequency.

An implication of these findings is the possibility that proper management of bubble size and release frequency enhances mass transfer and contributes to evenly distributed current density, resulting in lower overpotentials and improved electrolysis efficiency. In conclusion, this thesis highlights the importance of controlling bubble dynamics to overcome mass transport limitations and advance towards high current densities in alkaline water electrolysis.

Future Work

While the research characterized distinct aspects of bubbles behaviors in the transition to mass transport-dominated regime, none of the results showed a region associated with the limiting current density. To better comprehend the physics behind mass transport limitations, achieving higher current densities is required. However, due to the limited capacities of the lab-scale potentiostat used for this study, reaching the maximum reaction rate was restricted despite repeated attempts to reduce surface areas and increase current densities. Thus, future studies should explore the behavior of bubbles at higher current densities with an improved experimental configuration that allow for the input of higher potential and current.

Next, to improve the quality of event visualization, incorporating event-based cameras with pulsed illumination of high frequency could be beneficial. By projecting flashing light at high frequency, enhanced contrast and detection could be achieved, especially for the detection of objects in porous media. In addition, synchronizing flashing lights with event-based imaging data might enable more precise capture of bubble evolution processes. This method could potentially reduce motion blur and improve temporal resolution. Therefore, future research should focus on improving and validating these advanced imaging techniques to capture the complex interactions within electrochemical cells more effectively.

Reference

[1] Brauns J, Turek T. Alkaline water electrolysis powered by renewable energy: A review. Processes. 2020;8(2):248.

[2] Abe JO, Popoola A, Ajenifuja E, Popoola OM. Hydrogen energy, economy and storage: Review and recommendation. International journal of hydrogen energy. 2019;44(29):15072-86.

[3] Agency IE. Global Hydrogen Review 2023. International Energy Agency; 2023.

[4] Čučuk A. Hydrogen production to increase to 110 Mt per year by 2030, study says: Offshore Energy; 2023 [Available from: https://www.offshore-energy.biz/hydrogen-production-to-increase-to-110-mt-per-year-by-2030-study-says/#:~:text=The%20study%20revealed%20that%20global,neutral%20way%20using%20renewable%20energies.

[5] Zeng K, Zhang D. Recent progress in alkaline water electrolysis for hydrogen production and applications. Progress in energy and combustion science. 2010;36(3):307-26.

[6] Wang S, Shan S, Caracciolo D, Lu A, Robinson R, Shang G, et al. Nanoalloys and catalytic applications. Modeling, Characterization, and Production of Nanomaterials: Elsevier; 2023. p. 401-36.

[7] Shih AJ, Monteiro MC, Dattila F, Pavesi D, Philips M, da Silva AH, et al. Water electrolysis. Nature Reviews Methods Primers. 2022;2(1):84.

[8] Jiang W, Huang X, Ke W, Sheng L, Li J, Zhu F, et al. Tuning wettability of nickel-based electrode by micro-nano surface structure to boost OER catalysis. Journal of Alloys and Compounds. 2023;965:171367.

[9] Colli AN, Girault HH, Battistel A. Non-precious electrodes for practical alkaline water electrolysis. Materials. 2019;12(8):1336.

[10] Wan L, Xu Z, Xu Q, Pang M, Lin D, Liu J, et al. Key components and design strategy of the membrane electrode assembly for alkaline water electrolysis. Energy & Environmental Science. 2023;16(4):1384-430.

[11] Yuan S, Zhao C, Cai X, An L, Shen S, Yan X, et al. Bubble evolution and transport in PEM water electrolysis: Mechanism, impact, and management. Progress in Energy and Combustion Science. 2023;96:101075.

[12] Kumar SS, Lim H. An overview of water electrolysis technologies for green hydrogen production. Energy reports. 2022;8:13793-813.

[13] Ursua A, Gandia LM, Sanchis P. Hydrogen production from water electrolysis: current status and future trends. Proceedings of the IEEE. 2011;100(2):410-26.

[14] Taibi E, Miranda R, Carmo M, Blanco H. Green hydrogen cost reduction. 2020.

[15] Domalanta MR, Bamba JN, Matienzo DD, del Rosario-Paraggua JA, Ocon J. Pathways towards achieving high current density water electrolysis: From material perspective to system configuration. ChemSusChem. 2023;16(13):e202300310.

[16] Iwata R, Zhang L, Wilke KL, Gong S, He M, Gallant BM, et al. Bubble growth and departure modes on wettable/non-wettable porous foams in alkaline water splitting. Joule. 2021;5(4):887-900.

[17] Yuan S, Zhao C, Mei X, Shen S, Wang Q, Yan X, et al. Bubble management in PEM water electrolysis via imprinting patterned grooves on catalyst layer. International Journal of Heat and Mass Transfer. 2023;212:124249.

[18] Olivier P, Bourasseau C, Bouamama PB. Low-temperature electrolysis system modelling: A review. Renewable and Sustainable Energy Reviews. 2017;78:280-300.

[19] Angulo A, van der Linde P, Gardeniers H, Modestino M, Rivas DF. Influence of bubbles on the energy conversion efficiency of electrochemical reactors. Joule. 2020;4(3):555-79.

[20] Niroula S, Chaudhary C, Subedi A, Thapa B, editors. Parametric modelling and optimization of alkaline electrolyzer for the production of Green Hydrogen. IOP Conference Series: Materials Science and Engineering; 2023: IOP Publishing.

[21] Firtina-Ertis I. Thermodynamic and electrochemical assessment of an alkaline electrolyzer (AE) at different operating parameters. Journal of Environmental Chemical Engineering. 2022;10(2):107225.

[22] Dickinson EJ, Wain AJ. The Butler-Volmer equation in electrochemical theory: Origins, value, and practical application. Journal of Electroanalytical Chemistry. 2020;872:114145.

[23] Bard AJ, Faulkner LR, White HS. Electrochemical methods: fundamentals and applications: John Wiley & Sons; 2022.

[24] Zhao X, Ren H, Luo L. Gas bubbles in electrochemical gas evolution reactions. Langmuir. 2019;35(16):5392-408.

[25] Ikeda H, Misumi R, Kojima Y, Haleem AA, Kuroda Y, Mitsushima S. Microscopic high-speed video observation of oxygen bubble generation behavior and effects of anode electrode shape on OER performance in alkaline water electrolysis. International Journal of Hydrogen Energy. 2022;47(21):11116-27.

[26] Lee JK, Lee C, Fahy KF, Zhao B, LaManna JM, Baltic E, et al. Critical current density as a performance indicator for gas-evolving electrochemical devices. Cell Reports Physical Science. 2020;1(8).

[27] Mazloomi S, Sulaiman N. Influencing factors of water electrolysis electrical efficiency. Renewable and Sustainable Energy Reviews. 2012;16(6):4257-63.

[28] Darband GB, Aliofkhazraei M, Shanmugam S. Recent advances in methods and technologies for enhancing bubble detachment during electrochemical water splitting. Renewable and Sustainable Energy Reviews. 2019;114:109300.

[29] Park D-H, Park H-K, Chung B-J. Measurements of breakdown voltage and critical current density in a water electrolysis varying area and shape of working electrode. Journal of Electroanalytical Chemistry. 2023;928:117078.

[30] Park H-K, Chung B-J. Application of macrolayer dryout model for the critical current density of water electrolysis. International Communications in Heat and Mass Transfer. 2022;130:105759.

[31] Wei X, Kakimoto T, Umehara Y, Nakajima H, Ito K, Inagaki H, et al. Improvement of the critical current density of alkaline water electrolysis based on the hydrodynamic similarity between boiling and water electrolysis. International Journal of Heat and Mass Transfer. 2023;214:124420.

[32] Swiegers GF, Terrett RN, Tsekouras G, Tsuzuki T, Pace RJ, Stranger R. The prospects of developing a highly energy-efficient water electrolyser by eliminating or mitigating bubble effects. Sustainable Energy & Fuels. 2021;5(5):1280-310.

[33] Brandon N, Kelsall G. Growth kinetics of bubbles electrogenerated at microelectrodes. Journal of Applied Electrochemistry. 1985;15:475-84.

[34] Zhang D, Zeng K. Evaluating the behavior of electrolytic gas bubbles and their effect on the cell voltage in alkaline water electrolysis. Industrial & Engineering Chemistry Research. 2012;51(42):13825-32.

[35] Sakuma G, Fukunaka Y, Matsushima H. Nucleation and growth of electrolytic gas bubbles under microgravity. International journal of hydrogen energy. 2014;39(15):7638-45.

[36] Dastafkan K, Wang S, Song S, Meyer Q, Zhang Q, Shen Y, et al. Operando monitoring of gas bubble evolution in water electrolysis by single high-frequency impedance. EES Catalysis. 2023;1(6):998-1008.

[37] Qiu H, Obata K, Yuan Z, Nishimoto T, Lee Y, Nagato K, et al. Quantitative Description of Bubble Formation in Response to Electrolyte Engineering. Langmuir. 2023;39(14):4993-5001.

[38] Morales DM, Risch M. Seven steps to reliable cyclic voltammetry measurements for the determination of double layer capacitance. Journal of Physics: Energy. 2021;3(3):034013.

[39] Zheng W, Liu M, Lee LYS. Best practices in using foam-type electrodes for electrocatalytic performance benchmark. ACS Energy Letters. 2020;5(10):3260-4.

[40] Lake JR, Soto AlM, Varanasi KK. Impact of bubbles on electrochemically active surface area of microtextured gas-evolving electrodes. Langmuir. 2022;38(10):3276-83.

[41] Willert CE, Klinner J. Event-based imaging velocimetry: an assessment of event-based cameras for the measurement of fluid flows. Experiments in Fluids. 2022;63(6):101.

[42] Brändli CP. Event-based machine vision: ETH Zurich; 2015.

[43] Prophesee. EVK3 Prophesee Evaluation Kit Product Brief HD2. Prophesee; 2023.

[44] Fernandez D, Maurer P, Martine M, Coey J, Möbius ME. Bubble formation at a gas-evolving microelectrode. Langmuir. 2014;30(43):13065-74.

[45] Prophesee. Particle Size Measurement using Python [Available from: https://docs.prophesee.ai/stable/samples/modules/analytics/psm_py.html?highlight=particle%20size.

Appendix A: Synchronization of Data and Image

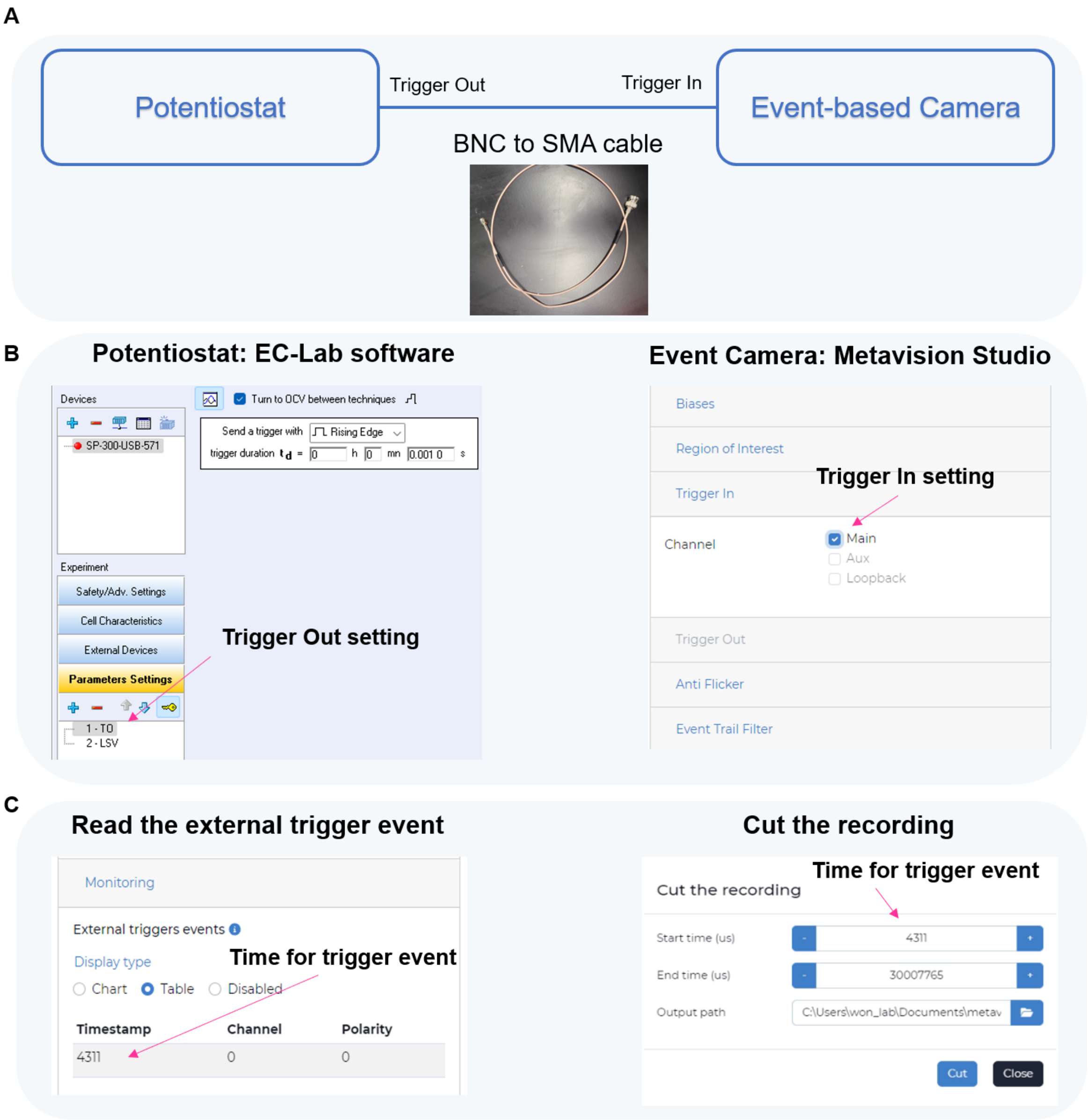

☑ Turn to OCV between techniques

Send a trigger with: Rising Edge

trigger duration t_d = 0 h 0 mn 0.001 0 s

Channel: ☑ Main ☐ Aux ☐ Loopback

External triggers events

Display type: ○ Chart ● Table ○ Disabled

Timestamp	Channel	Polarity
4311	0	0

Cut the recording

Start time (us): 4311

End time (us): 30007765

Output path: C:\Users\won_lab\Documents\metav

Figure A. Synchronization of Data and Image

(A) Physical connection via a BNC to SMA cable between a potentiostat and an event-based camera. (B) Software setting for trigger-out and trigger-in: EC-lab software for trigger-out (left), Metavision Studio software for trigger-in(right). (C) Post-processing for cutting the recording with a trigger event

Appendix B: Bubble Count and Size Measurement

All measurements for bubble count and diameter were performed using the "Particle Size Monitoring" analytic tool in Metavision SDK, provided by Prophesee. The parameters used for the measurement in this study are as follows: accumulation time (2000 μs), precision time (220 μs), cluster threshold (5), number of cluster threshold (5), polarity (OFF), and learning rate (1). This set of parameters was determined by repeatedly adjusting them to approximate to ground truths. The average percentage difference between the ground truth and the measure data is 4.3% for size measurement and 13.5% for bubble count.

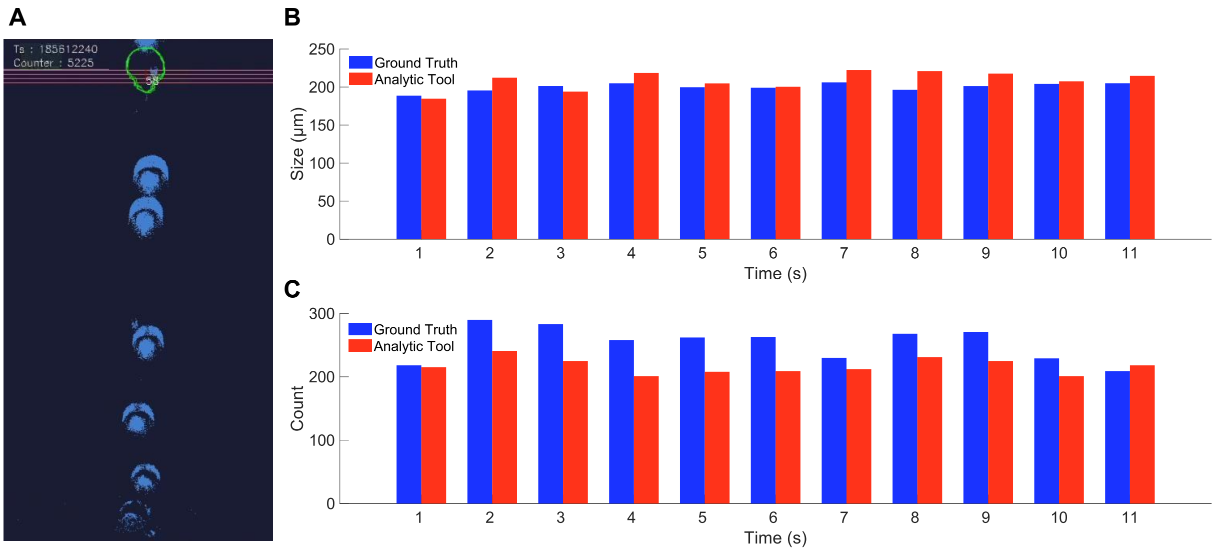

Figure B. Bubble Count and Size Measurement.

The image (A) shows a demonstration of the analytic tool. When a bubble passes over the red lines, the algorithm detects its contour and calculate its size. The detailed description of how the algorithm works can be found on Prophesee's official website [45]. The bar graphs in (B) and (C) compares the ground truth data with the results acquired via the analytic tool. The validation was performed with a video of nickel foam over 11 seconds.

Appendix C: Tafel Plots for Porous Nickel Foam

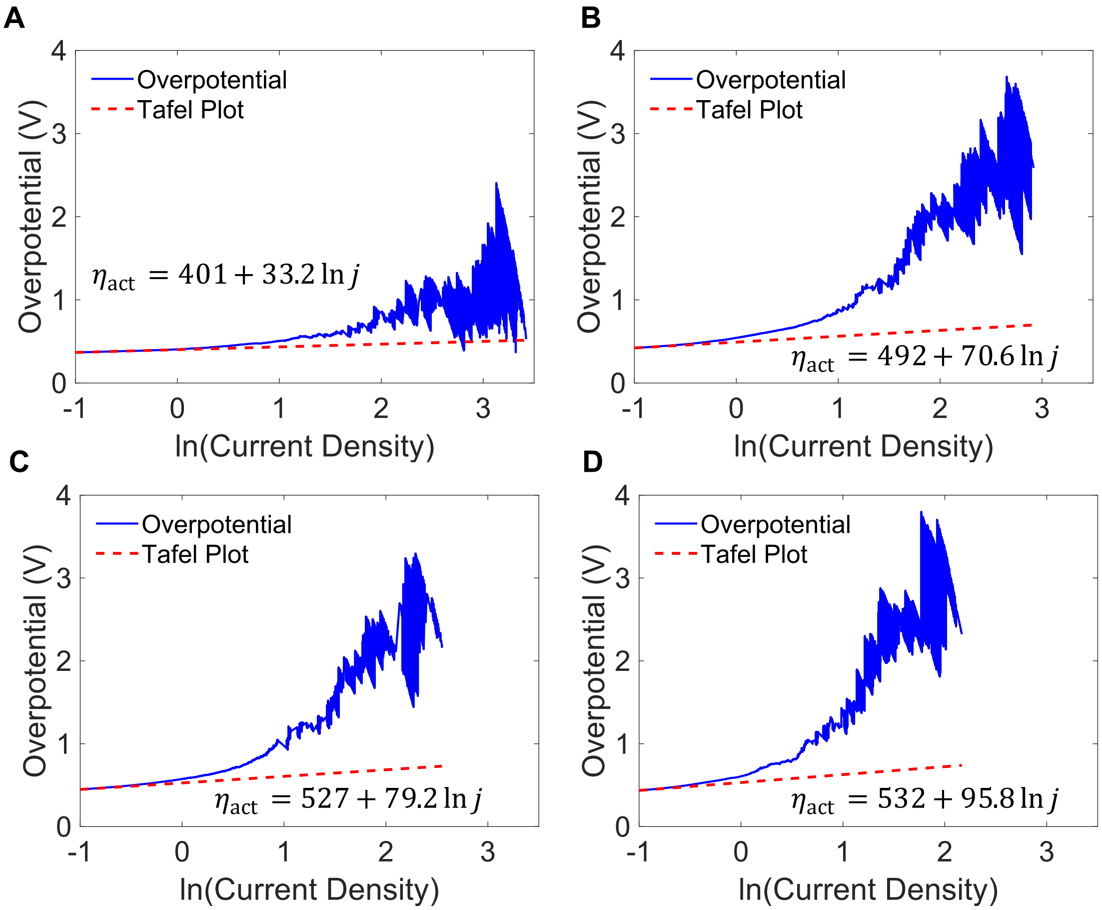

Figure C. Tafel plot to the overpotential versus logarithmic current density

The Tafel fitting was performed over the logarithmic current density range of -1.2 to -0.9, where the data exhibited a linear region. (A) 10 mm x 3 mm. (B) 10 mm x 10 mm. (C) 10 mm x 20 mm. (D) 10 mm x 25 mm.

Appendix D: Experimental Results for Copper Wire

Electrochemical Investigation

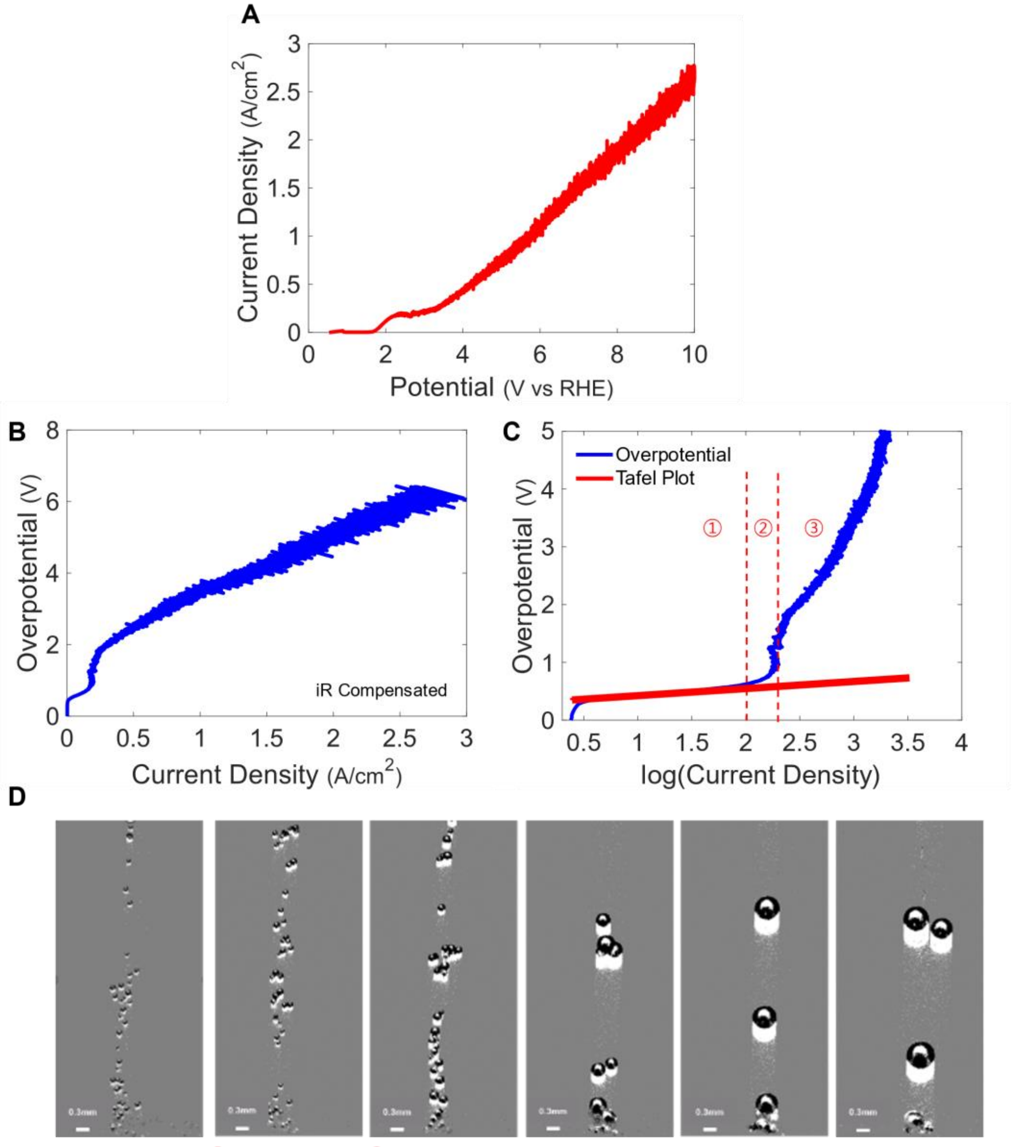

① ~ 0.1 A/cm^2 ② 0.1~0.16 A/cm^2 ③ 0.16~0.24 A/cm^2 0.7 A/cm^2 1.4 A/cm^2 2.3 A/cm^2

Figure D1. Electrochemical Characterization of a Copper Wire

(A) Polarization curve. (B) Overpotential as a function of current density (A/cm^2) with iR compensation. (C) Tafel plot to the overpotential versus logarithmic current density (mA/cm^2). The Tafel fitting was conducted beyond logarithmic current density of 0.5, where the data exhibited a linear region. (D) Event-based Images taken during the reaction.

Overpotential Analysis

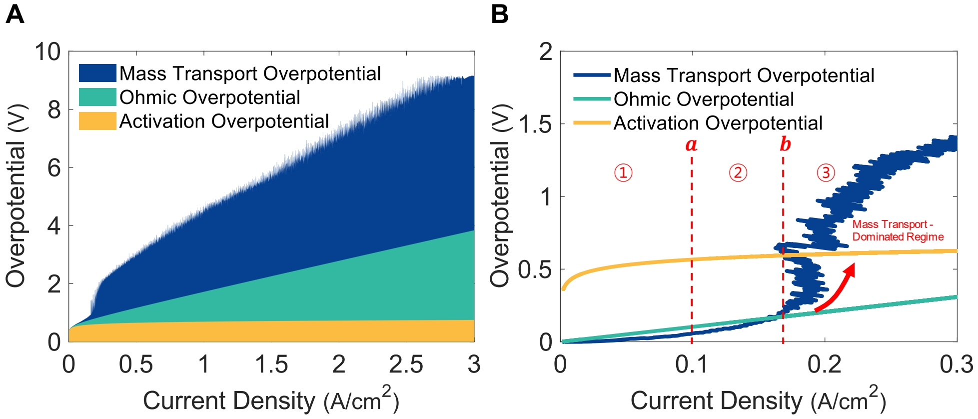

Figure D2. Overpotential Analysis of a Copper Wire.

(A) Decomposition of total overpotential into its individual components: Activation overpotential, Ohmic overpotential, and Mass transport overpotential. (B) Transition toward a mass transport-dominated regime.

Oxygen Bubble Behavior

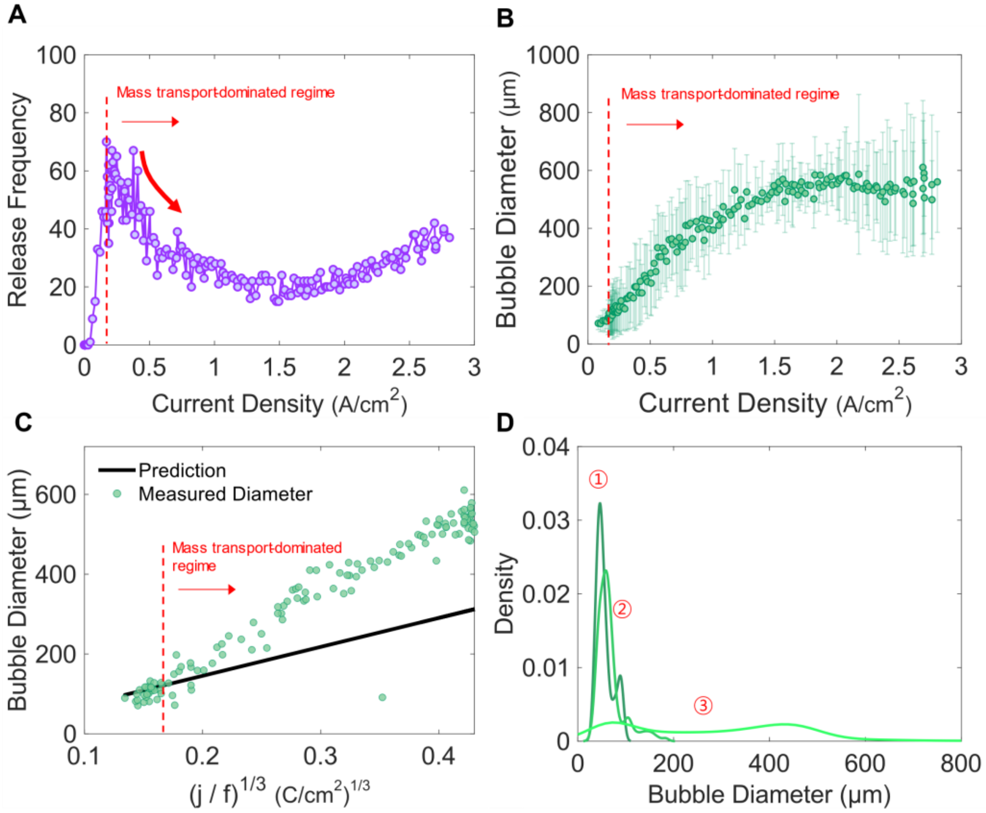

Figure D3. Analysis of Bubble Dynamics at a Copper Wire.
(A) Variation of bubble release frequency with current density. (B) Bubble diameter as a function of current density. (C) Comparison of measured and predicted bubble diameter [Appendix E]. (D) Kernel density estimation of bubble diameter distributions

Fluctuation Analysis

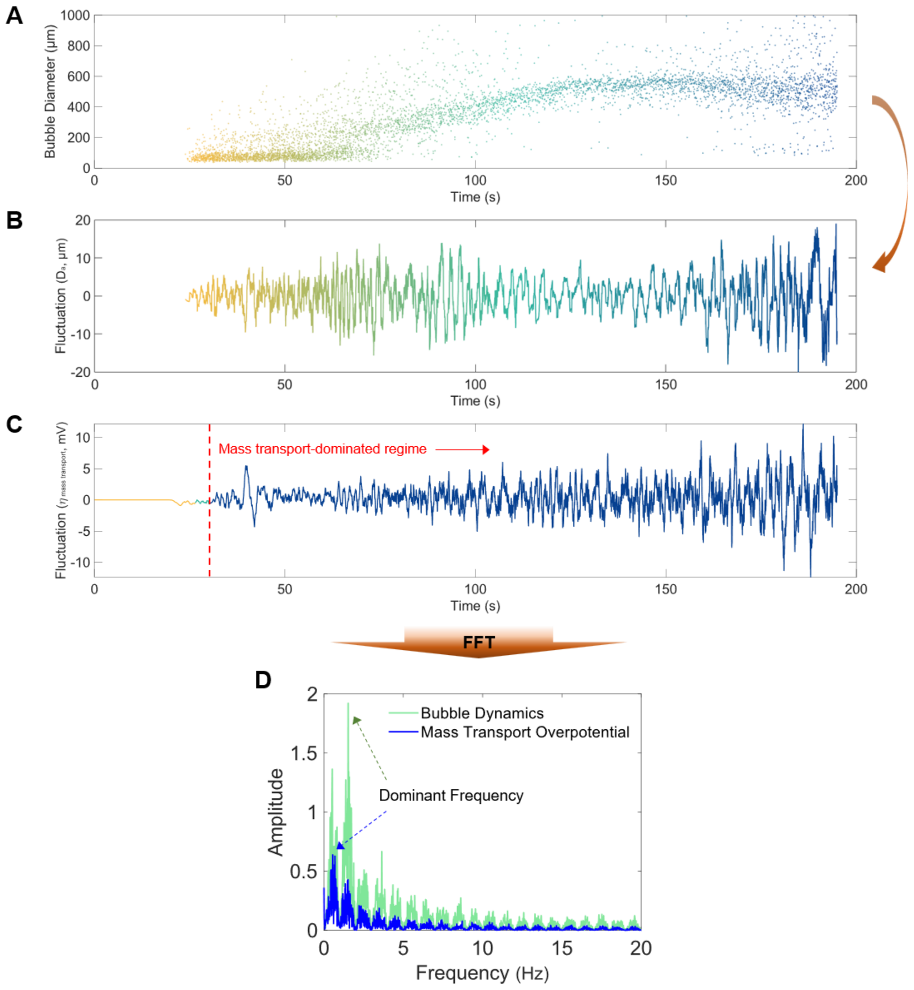

Figure D4. Frequency Analysis of Bubble Dynamics and Overpotential.
(A) Temporal evolution of bubble diameter. (B) Fluctuations in bubble diameter over time. (C) Fluctuations in mass transport overpotential over time. (D) Frequency domain analysis: bubble dynamics vs. mass transport overpotential. The fluctuations were analyzed by removing long-term trends from the data, leaving the remaining variations. For the detrending, STL decomposition (Seasonal-Trend decomposition using Loess) method was used.

Appendix E: Prediction of Bubble Departure Diameter [44]

Bubble departure diameter can be predicted using the release frequency (f) and the measured current (i) in the equation of the gas law:

$$PV = nRT$$

It is assumed that all oxygen gas forms bubble in a completely spheric shape and only atmospheric pressure is considered for the pressure inside the bubble. The ideal gas equation can be modified to the following equation:

$$P_0 \cdot \left(\frac{\pi d^3}{6}\right) = \left(\frac{i}{fzF}\right) \cdot RT$$

where d is the bubble diameter i is the current, f is the release frequency, z is the number of electrons involved in the reaction ($z = 4$, oxygen evolution reaction), F is the Faraday's constant (96,485 C/mol), R is the gas constant (8.314 $J/(mol \cdot k)$), P_0 is the atmospheric pressure ($10^5\ N/m^2$), T is the temperature in Kelvin.

Finally, bubble departure diameter can be predicted using the equation below:

$$d = (\frac{1.5iRT}{fFP\pi})^{\frac{1}{3}}$$

In this study, the bubble diameter measured via an event-based camera is compared with the predicted diameter to validate the data.

Appendix F: Analysis of Current and Bubble Dynamics

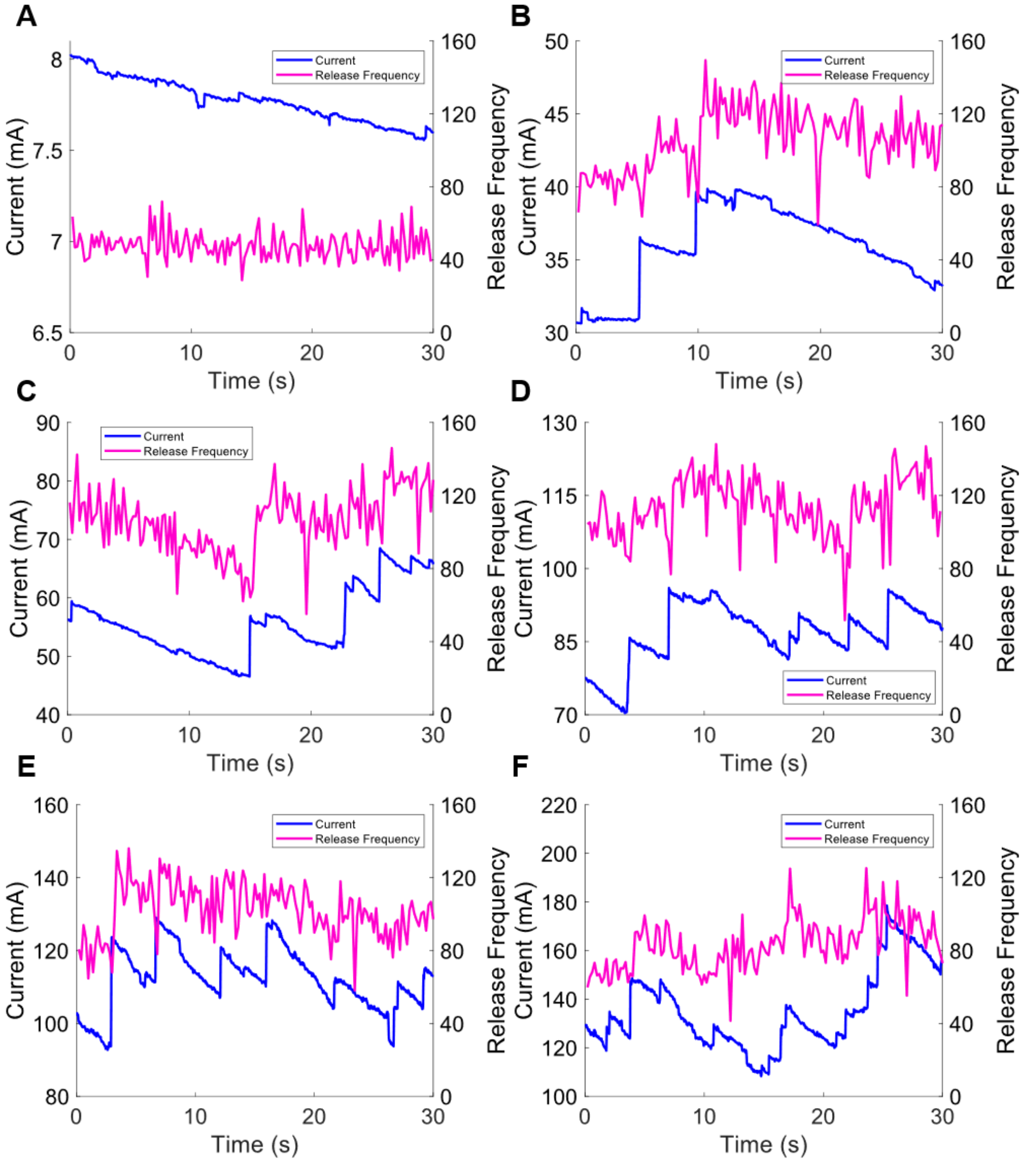

Figure F1. Comparison of Current and Release Frequency.

Both the current and the release frequency data was collected synchronously during chronoamperometry measurements. The recorded period is 30 seconds. The potential range is from 1 V to 6 V, with an interval of 1 V (A~F). The variations in both data are very similar.

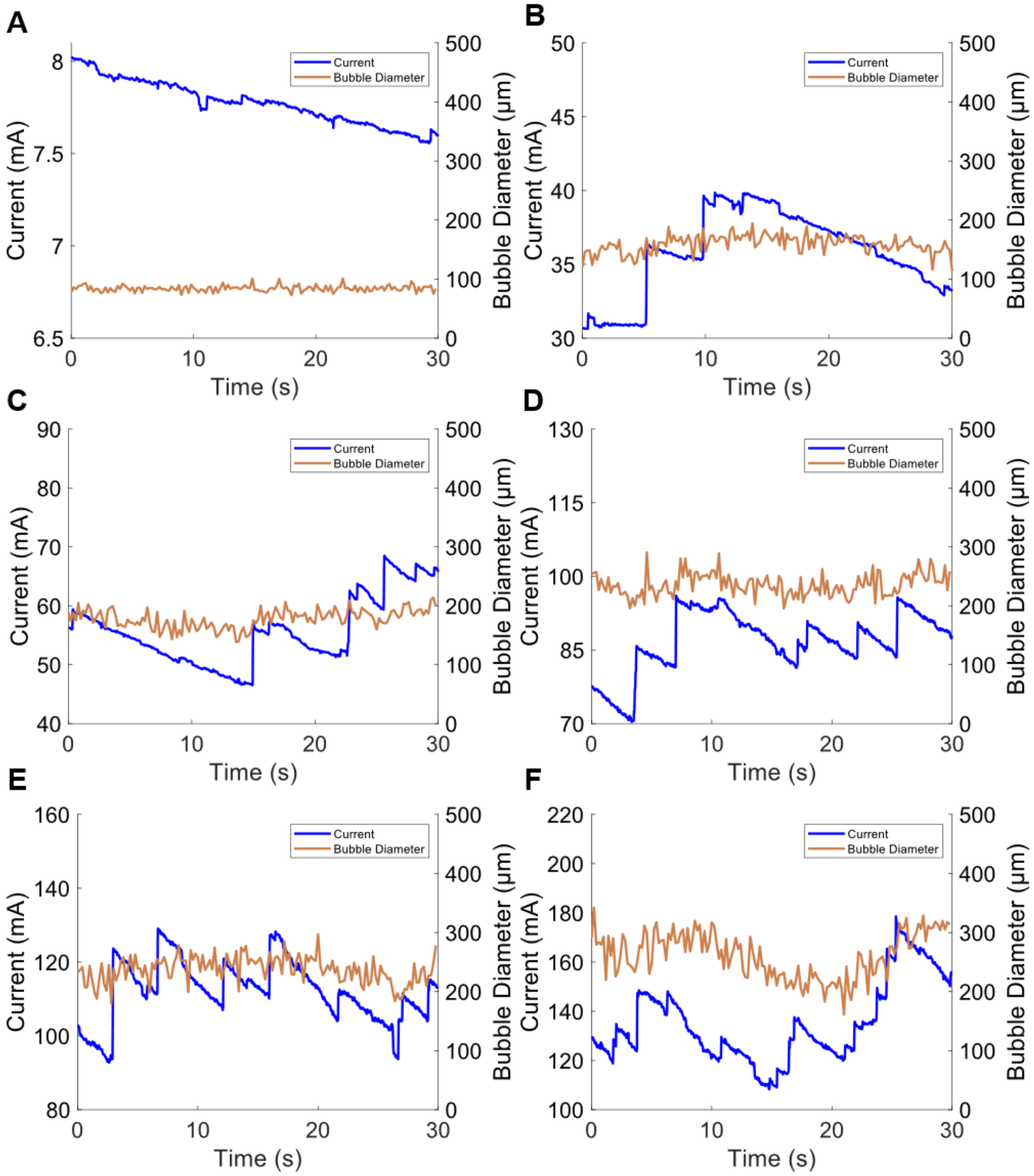

Figure F2. Comparison of Current and Bubble Diameter.

Both the current and the bubble diameter data were synchronously collected during chronoamperometry measurements for 30 seconds. The potential range is from 1V to 6V, with an interval of 1 V (A~F). The variations in both data are not that similar, compared to the release frequency. Plot F displays slightly the similar trend.